A PCA-based framework for determining remotely-sensed geological surface orientations and their statistical quality

Daven P. Quinn[1] and B.L. Ehlmann[1,2]

[1]Division of Geological and Planetary Sciences, California Institute of Technology, Pasadena, California, USA Correspondence to lead author: davenquinn@alumni.caltech.edu
[2]Jet Propulsion Laboratory, California Institute of Technology, Pasadena, California, USA

June 19, 2018

This preprint manuscript is under review at Earth and Space Sciences. Initial submission: May 2018

Abstract

The orientations of planar rock layers are fundamental to our understanding of structural geology and stratigraphy. Remote-sensing platforms including satellites, unmanned aerial vehicles (UAVs), and LIDAR scanners are increasingly used to build three-dimensional models of structural features on Earth and other planets. Remotely-gathered orientation measurements are straightforward to calculate but are subject to uncertainty inherited from input data, differences in viewing geometry, and the regression process, complicating geological interpretation. Here, we improve upon the present state of the art by developing a generalized means for computing and reporting errors in strike-dip measurements from remotely sensed data. We outline a general framework for representing the error space of uncertain orientations in Cartesian and spherical coordinates and develop a principal-component analysis (PCA) regression method which captures statistical errors independent of viewing geometry and input data structure. We also build graphical techniques to visualize the uniqueness and quality of orientation measurements, and a process to increase statistical power by jointly fitting bedding planes under the assumption of parallel stratigraphy. These new techniques are validated by comparison of field-gathered orientations with minimally-processed satellite imagery of the San Rafael Swell, Utah and UAV imagery from the Naukluft Mountains, Namibia. We provide software packages supporting planar fitting and the visualization of error distributions. This method provides a means to increase the precision and comparability of structural measurements gathered using a new generation of remote-sensing techniques.

Key Points

- A new statistical framework allows the error analysis of orientations of geologic planes and visualization of errors.
- Principal component analysis flexibly responds to different sources of error and supports joint fitting of parallel sedimentary bedding.
- The software workflow supporting error analysis and visualization can be used with terrestrial and planetary data at a variety of scales.

Contents

1 Introduction

The orientations of geological features such as faults, dikes, lava flows, and sedimentary beds record characteristics of deposition or emplacement, episodes of deformation, and relationships between bodies of rock. Idealized planes describing these features are common units of geological analysis. Planar orientations have most often been collected directly, using a field structural compass or surveying equipment. The increasing viability of high-resolution remote-sensing techniques has allowed three-dimensional imaging of geological features at sub-meter scale.

In field mapping by a structural geologist, directly-measured orientations (e.g. using a pocket transit on outcrops) have been considered sufficiently accurate that errors are not reported. Orientations measured using remotely-gathered data are a powerful new tool for geological analysis, especially when outcrops are inaccessible to direct measurement. However, poorly-modeled and hard-to-visualize errors complicate the process of arriving at the true orientation of a geological structure. Remote-sensing datasets can spatially vary in resolution and quality, and measurements are potentially biased by terrain effects, sensor-dependent noise, measurement geometry, and operator error in defining relevant features, among other sources of error.

One major motivation of this work is the orbital mapping of layered rocks on Mars, which are key indicators of Mars' geological history (e.g. *McEwen et al.*, 1999; *Malin and Edgett*, 2000; *Quantin et al.*, 2005; *Dromart et al.*, 2007; *Lewis et al.*, 2008a; *Stack et al.*, 2015). For example, sedimentary deposits are mapped from orbit and with rovers, but detailed evaluation of their depositional mechanisms requires understanding bedding orientations, particularly bedding dip (e.g. *Lewis and Aharonson*, 2006, 2014; *Lewis et al.*, 2008b; *Okubo et al.*, 2008; *Okubo*, 2010; *Edgar et al.*, 2012; *DiBiase et al.*, 2013; *Kite et al.*, 2013; *Goudge et al.*, 2017; *Quinn and Ehlmann*, 2018, submitted). Detailed accounting for errors is also important in large-scale regional studies, where variable data resolution and outcrop quality affect the dataset (e.g *Metz et al.*, 2010).

At present, some Mars mapping studies report no error ranges (e.g. *DiBiase et al.*, 2013) while others report bedding orientations with error ranges output from commercial regression packages (e.g. *Okubo et al.*, 2008). Other studies use "dip error" (*Lewis and Aharonson*, 2006; *Goudge et al.*, 2017), "pole error" (*Kite et al.*, 2016), or bootstrap resampling statistics (*Metz et al.*, 2010; *Fraeman et al.*, 2013) to evaluate measurement quality. The varying approaches used to generate orientation errors, along with different degrees of reporting rigor, complicate understanding of the accuracy and precision of specific strike-dip measurements and consequent implications for the geologic structure.

Even carefully-planned structural studies with consistent error analysis procedures cannot be easily interpreted using current visualization tools. For instance, map symbols for nominal strike and dip do not provide a means of understanding commonly unpredictable, nonlinear errors inherent in orientation measurements in varied terrain, and individual orientation measurements often only coarsely correspond to the overall structural pattern (e.g. *Lewis and Aharonson*, 2006;

Okubo et al., 2008; *Quinn and Ehlmann*, 2018, submitted). Without methods to visualize orientation certainty, reported bedding orientations do not fully communicate information used in study interpretations.

The use of remotely-sensed orientation measurements in terrestrial geology is also a key driver of this work. High-resolution satellite imagery and DEMs are now available for much of the Earth's surface (e.g. *Gesch et al.*, 2014), supporting regional photogeologic mapping. The advent of field-portable Light Detection and Ranging (LIDAR) instruments (*Buckley et al.*, 2008) and the improving accuracy of structure-from-motion (SfM) photogrammetry support the increasing remote measurement of geological surface orientations. Numerous recent studies use orientation measurements from unmanned aerial vehicle (UAV) photogrammetry (e.g. *Vollgger and Cruden*, 2016), often using three-point analytical approximations (*Fienen*, 2005) or commercial regression packages.

Terrestrial datasets are often hindered by the same factors complicating analyses on Mars. For example, in a recent study of the accuracies of remotely derived data, *Cawood et al.* (2017) extract bedding planes and fold axes from LIDAR and SfM photogrammetric digital surface models of weathered beds of the Stackpole syncline that are comparable with high accuracy to direct measurements in most cases. However, significant difference in fit were found between LIDAR, ground-, and UAV-based photogrammetry that were related to the orientation of the outcrop and viewing geometry as well as the scale of facet construction and point fitting.

Improvements on the state-of-the-art in computing and visualizing error methods must include several factors. Bedding orientation measurements depend not only on the internal errors of the remote-sensing dataset but also on the geometry of the outcrop measured (e.g. hillslope concavity and aspect) and accuracy in following bedding features. Measurements from the same dataset and geologic unit can have completely different error structures depending on the shape of topography, presenting a challenge for error analysis. A statistical and data-visualization framework designed for planar orientation measurements will enable quantitative comparison between planar fits with completely different error structures. By increasing the robustness of orientation determination from heterogeneous data, such a framework extends the range of situations in which structural metrics can be reliably assessed from remote-sensing imagery, enabling statistically rigorous comparison of measurements with a wide variety of source data type, outcrop exposure and quality, and viewing geometry.

The methods developed in this study to improve the calculation and visualization of orientation errors were developed in conjunction with structural mapping of the layered sulfates at northeast Syrtis Major, Mars. These thick layered deposits occupy a critical stratigraphic interval, but their relatively poor exposure complicates orientation measurement. Additionally, because small changes in dip can imply completely different depositional processes, high-confidence angular measurements are crucial drivers of interpretation (*Quinn and Ehlmann*, 2018, submitted).

Here, we detail the developed method. First, we describe a generalized approach to planar orientation errors for three-dimensional datasets [Section 2] and its implementation as a PCA-based statistical procedure for planar fitting [Section 3]. We test the method using terrestrial orientations recovered from satellite and UAV data [Section 4] and discuss potential alternative statistical parameterizations [Section 5]. Finally, we describe general geometric transformations for the error space of a plane [Section A] and several open-source software packages supporting planar fitting and error visualization for orientation data.

2 Background: the structure of a remotely-sensed plane and its error space

A geologic surface is typically extracted from remote-sensing data by isolating representative points into a three-dimensional point dataset. A common procedure is the extraction of elevation for points along a bedding trace digitized from visible imagery and overlain on a gridded elevation model. Related procedures include the grouping of closely-spaced LIDAR points sampling the same surface (e.g. *Weingarten et al.*, 2004) or direct elevation measurement along a feature trace by theodolite or differential GPS. Since remote-sensing datasets are typically defined in Cartesian spatial coordinates, all of these methods produce an array of three-dimensional points in space that collectively represent a single feature.

Regression is the key method for extracting planar representations of geological surfaces from their spatial extent. The set of coordinates that represents a potential plane is converted to an orientation by finding the best-fitting plane through the dataset using minimization (e.g. PCA, OLS, and other regression frameworks) in Cartesian coordinate space (*Fahrmeir et al.*, 2013; *Jolliffe*, 2002). The idealized geologic surface that results from regression can be mathematically described as a plane, requiring three free parameters. Description of orientation alone requires only two free parameters, represented either as slopes in two directions or the orientation of a normal vector to the plane [Figure 1a].

Regression of a best-fitting plane inherently involves uncertainty, which combines with irregularities in the input dataset to produce orientation errors. In Cartesian space terms, these errors can be represented as a hyperboloid of two sheets enclosing all possible planes in the dataset, varying around the nominal regression line, or alternatively as a set of normal vectors perpendicular to the plane. Assuming a fixed length, the error space for this normal vector forms an ellipsoid containing possible vector endpoints [Figure 1b].

In spherical coordinates, orientations are intuitively represented as a pair of angles (commonly, strike/dip, or dip/dip-direction). This two-angle representation supports visualization of orientation information on stereonets and related spherical plots. Previous studies of bedding orientation errors have parameterized orientation error in terms of strike and dip (*Cruden and Charlesworth*, 1976), and many workers have reported orientation errors in these terms (e.g.

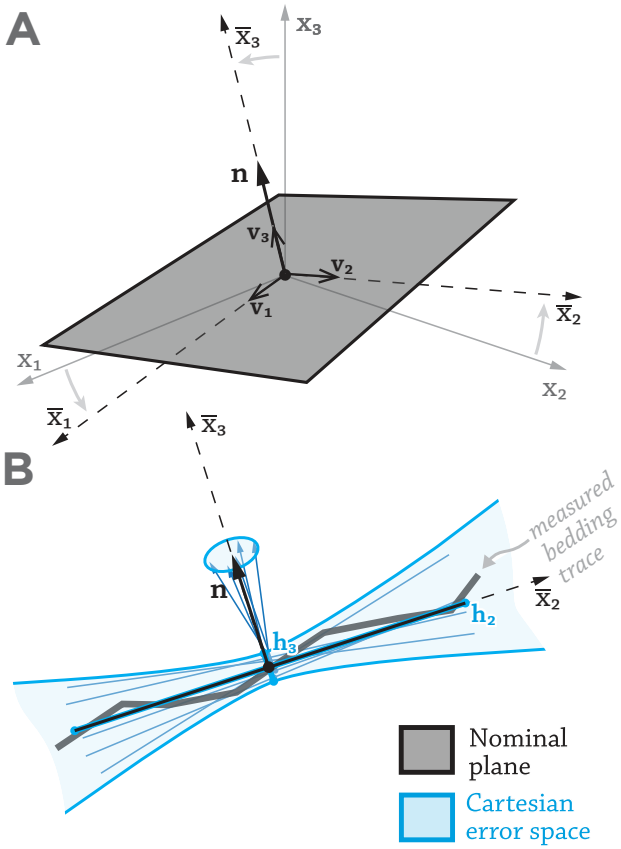

Figure 1: Schematic representation of the structure of a plane with errors and its relation to the global Cartesian coordinate system $\mathbf{x}$. **(a)** The plane and its associated normal vector $\mathbf{n}$. In unweighted PCA, $\mathbf{n}$ falls along the principal component axis $\overline{\mathbf{x}}_3$. The three unit vectors $\mathbf{v}_i$, oriented along $\overline{\mathbf{x}}_i$, form rows of the rotation matrix $\mathbf{V}$ that maps $\mathbf{x}$ to $\overline{\mathbf{x}}$. **(b)** A $\overline{\mathbf{x}}_2$-$\overline{\mathbf{x}}_3$ slice of the nominal plane and its normal vector, along with a bundle of planes with slightly different orientations and the encompassing hyperbolic error space (blue).

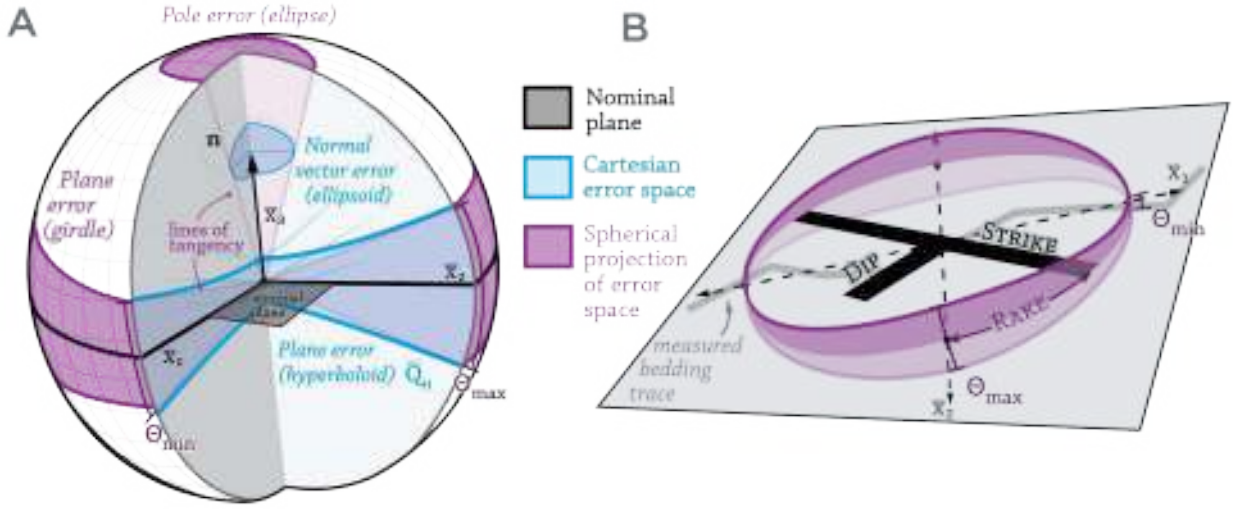

Figure 2: Schematic representation of the relationship between the nominal planar fit *(black)*, the hyperbolic error shell $\overline{\mathbf{Q}}_\mathbf{H}$ and inverse ellipsoid representing the normal vector endpoint *(blue)*, and the spherical error distribution formed by projecting the tangents to these error spaces onto the unit sphere *(purple)*. θ_{min} and θ_{max} define the scale of orientation errors along two axes within the plane, $\overline{\mathbf{x}}_1$ and $\overline{\mathbf{x}}_2$. **(a)** Projection of Cartesian error space to spherical coordinates, both as a planar girdle and pole error ellipse. **(b)** Orientation of the error space to the plane (defined by θ_{min} and θ_{max}) relative to the nominal plane, emphasizing the *rake* angle needed to report the directions of errors within the plane.

Table 1: Classification of dataset major axes

Scenario[a]	Hyperbolic axes[b]	Shape of variance ellipsoid	Notes
A	$\mathrm{h}_1 \approx \mathrm{h}_2 > \mathrm{h}_3$	Prolate ellipsoid	Plane well-defined in two dimensions, with small error axis
B	$\mathrm{h}_1 > \mathrm{h}_2 > \mathrm{h}_3$	Scalene ellipsoid	Quality of planar fit depends on axial dimensions and structure of dataset
C	$\mathrm{h}_1 > \mathrm{h}_2 \approx \mathrm{h}_3$	Oblate ellipsoid	Defined along a line, but with no unique planar orientation
D	$\mathrm{h}_1 \approx \mathrm{h}_2 \approx \mathrm{h}_3$	Spherical	Poorly constrained on all axes, no clear plane defined

[a] Scenario lettering corresponds to Figures 4, 5, and 6.
[b] $\mathbf{h} = \boldsymbol{\lambda}$ in *Onstott* (1980), and $\mathbf{h} = \boldsymbol{\lambda} + F\boldsymbol{\sigma}_{\boldsymbol{\lambda}}$ in this work (see Table 3 for notation definition).

Lewis and Aharonson, 2006; *Okubo et al.*, 2008). However, orientation errors are not necessarily aligned with the strike/dip parameters that describe the nominal plane, and errors expressed in terms of strike/dip rely implicitly on the small-angle assumption. Near-horizontal bedding (a common mode of stratigraphic exposure) has highly nonlinear angular dispersion in strike when approaching zero dip, with large covariances between the two.

Errors parameterized as pole error (angular error around the nominal orientation of a plane) yield error cones that are not subject to linearization error, however, the magnitudes of these pole errors must be defined with a statistical process. Directional statistical fitting mechanisms commonly used for geological orientations yield errors parameterized as pole error but operate entirely on data already expressed in angular terms (e.g. *Bingham*, 1974; *Onstott*, 1980; *Kent et al.*, 1983; *Fisher et al.*, 1987; *Mardia*, 2014).

Regression errors defined in Cartesian space can be mapped to spherical coordinates using geometric projection. Hyperbolic and ellipsoidal error spaces to a planar fit in Cartesian coordinates can be projected on a unit sphere: hyperbolic errors to the plane map to a spherical girdle (a bundle of great circles), and normal vector errors project to an ellipse [Figure 2a]. The angular span of this spherical girdle or ellipse can be defined by θ_{max}, the maximum angular error to the plane, and θ_{min}, which is orthogonal to θ_{max} by definition (and spatial reasoning). θ_{max} need not be oriented along strike or along dip; instead, the orientation of θ_{max} with respect to the nominal plane is expressed using a *rake* angle between the strike of the plane and θ_{max} [Figure 2b]. This format generalizes pole error to allow the full expression of a Cartesian orientation error space in angular terms, with five free parameters. This error structure forms the foundation for this work.

3 Methods

3.1 PCA for planar fitting

3.1.1 Error treatment in OLS vs. PCA OLS regression is the most common technique for fitting orientations of lines and planes. However, many other regression techniques exist which chiefly differ in their mechanism for apportioning error along the coordinate axes of the fit. Many of these parameterizations can be used to define errors to a plane. In PCA, the focus of this study, errors are fitted orthogonal to the best-fitting plane.

OLS regression fundamentally tests the relationship of a dependent variable with a set of independent variables. All error is assumed to belong to the independent data, which in spatial data is usually assigned to the vertical plane. This property inhibits the fitting of steep slopes [Figure 3]. Geological planes are often expected to be steeply dipping, depending on their origin and geologic context, and the assumption that errors are chiefly vertical is not always reasonable.

Unlike OLS, PCA fits errors along all axes simultaneously, with no distinction between independent and dependent data. This is a significant advantage for fitting arbitrarily-oriented planes atop datasets with different error structures. For instance, errors for photogrammetric datasets are generally dependent on the viewing geometry of the image pair(s) used to assemble the 3D model; elevation models created from oblique UAV imagery of cliff faces e.g. 4.2 will have chiefly horizontal errors, and multi-view SfM datasets will have errors oriented along arbitrary, oblique view planes. This variability of error structure in a scene requires a flexible fitting mechanism that can incorporate off-vertical errors. Even elevations measured on a gridded dataset have several sources of non-vertical error: (1) error in the construction of the DEM (e.g. photogrammetric image-registration error), (2) resampling error (sub-post smoothing imparted by gridding) (3) sampling error (inexact digitization of measured features), and (4) downslope bias. Though often poorly quantified, these errors still influence the output of planar fitting. The PCA technique has been used for planar fitting in contexts ranging from paleomagnetism (*Kirschvink*, 1980) to computer vision and depth-mapping, where orientation flexibility is required to map features such as vertical walls (*Weingarten et al.*, 2004; *Nurunnabi et al.*, 2012).

Much of the literature urges caution when applying PCA to estimate statistical confidence (e.g. *Faber et al.*, 1993, 1995; *Jolliffe*, 2002). PCA is not usually developed or motivated with a clear probabilistic framework (*Tipping and Bishop*, 1999), and is instead commonly used as a tool for dimensionality reduction, compressing the variation of a multidimensional dataset into a smaller set of explanatory variables. That process is difficult to statistically model, largely limiting PCA to algorithmic applications (e.g. image processing) and exploratory data analysis, except where explicit statistical rationale can be advanced for how many principal components to retain (*Jolliffe*, 2002). For the fitting of spatial planes, both input and output data are tied to orthonormal spatial coordinates, and finding the best-fitting plane involves only rotation, not dimensionality reduction, allowing us to circumvent this source of uncertainty. Evaluating the orientation and scatter along the axes of the input data, rather than discarding some of them, is statistically straightforward [Section 3.3].

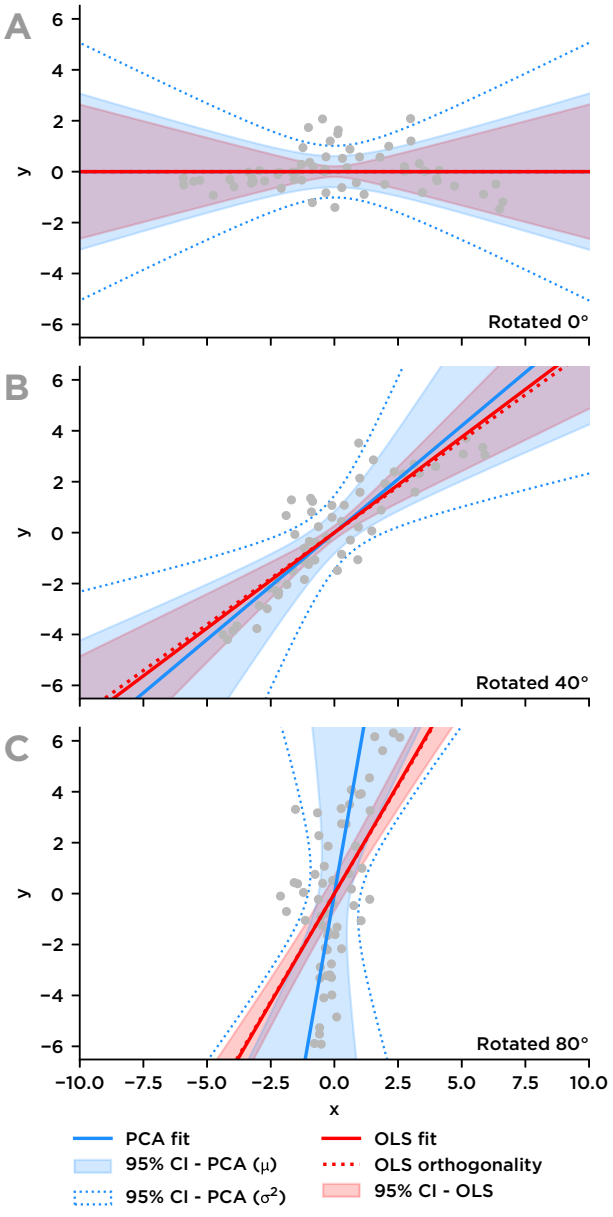

Figure 3: PCA and OLS regressions of a 2-dimensional, zero-centered point cloud rotated counterclockwise by **(a)** 0°, **(b)** 40°, and **(c)** 80°, emphasizing the nonlinear relationship between OLS and PCA regressions for differently-dipping planes with the same measurement scatter. Unweighted PCA retains the same error structure regardless of orientation, while the scale of OLS errors decrease as fitted orientations steepen. OLS is also structurally unwilling to fit near-vertical data. When it is not rigorously known that errors occur only in the vertical plane, PCA provides more potential to reconstruct orientation data.

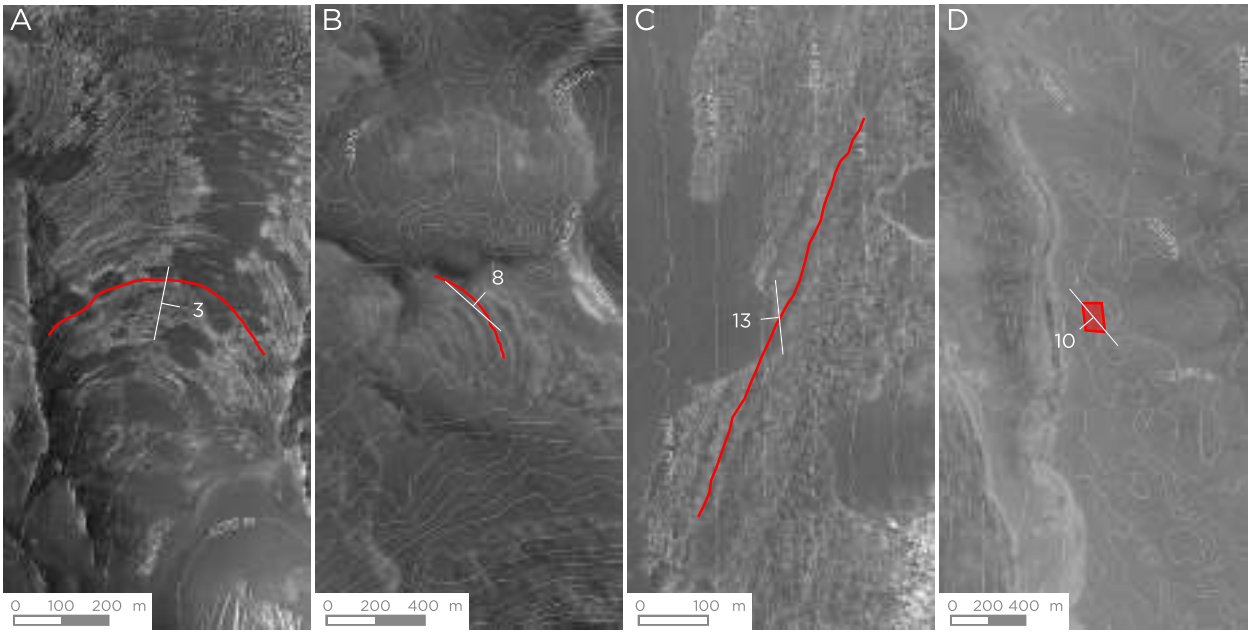

Figure 4: Context maps showing traced bedding planes (red) and nominal calculated bedding orientations for four orientation measurements in the NE Syrtis region of Mars. Imagery backdrop is HiRISE or CTX imagery, and 10 m contours derived from photogrammetry on the same dataset show the elevation data used to extract orientations. **(a)** a bedding exposure on a concave hillslope between two parallel raised ridges, atop a HiRISE image and elevation model. **(b)** A similar concave hillslope with slightly less 3D exposure, atop lower-resolution CTX data. **(c)** A linear bedding trace on a planar, west-facing hillslope. **(d)** A rectangular area of a dipping lava flow surface atop low-precision CTX topography.

3.1.2 Orientation examples To exhibit the properties of the PCA algorithm applied to datasets of varying quality, we focus on four endmember type examples of digitized bedding traces [Figure 4] with a range of dataset structures corresponding to Table 1. These examples are digitized traces of sedimentary bedding measured within an area in NE Syrtis, Mars during the study described in *Quinn and Ehlmann* (2018). Orientations were collected atop paired orthophotos and DEMs, which have different spatial resolutions and error structures due to to variable dust cover and stereo geometry. Additionally, these bedding traces cover a range of hillslope aspect and curvature, allowing them to query a wide range of potential error structures. We follow these bedding traces through transformation of their error space from Cartesian to spherical coordinates, and the numerical breakdown of their errors is summarized in Table 2.

3.2 The nominal plane in PCA

3.2.1 Notation Matrices are uppercase and bold ($\mathbf{M}$), while vectors are lowercase and bold ($\mathbf{x}$). Vector components use upright characters (x_1) while scalar quantities are in script (n). The subscript i defines a range of indices over the dimensions of the coordinate basis $i = [1, 2, 3]$. Thus $\mathbf{x} = \mathrm{x}_i = [\mathrm{x}_1, \mathrm{x}_2, \mathrm{x}_3]$. When a vector component is given in subscript (e.g. σ_λ), its implicit i index is dropped. An index of all notation is contained in Table 3.

Table 2: Data for orientation examples

			Eigenvalues			Spherical summary (°)				
n	L[1]	R[2]	λ_1	λ_2	λ_3	strike	dip	rake	θ_{min}	θ_{max}
Type examples [Table 1, Figures 5 and 6, ordered a-d]										
31	479	2.0	17228	422.9	0.82	311.7	7.6	81.5	0.59	3.88
546	584	1.1	21634	2079.3	0.11	11.3	3.5	172.7	0.15	0.48
593	615	2.4	31514	10.0	0.66	174.2	13.2	60.9	0.29	16.49
172	0	18.5	2163	948.1	73.74	139.6	10.1	119.2	13.17	19.92
Joint fitting of parallel planes [Figure 8]										
Well-constrained single-bed measurements										
476	507	0.7	16825	1437.8	0.09	9.3	3.5	9.9	0.15	0.51
546	584	1.1	21634	2079.3	0.11	11.3	3.5	172.7	0.15	0.48
Joint fit										
1217	–	1.3	6431	972.4	0.13	11.8	3.5	156.1	0.28	0.71
Components (ordered from north to south)										
315	332	0.5	8940	88.1	0.05	339.7	3.5	167.7	0.15	1.54
189	209	1.1	3544	14.1	0.09	38.3	6.7	112.5	0.34	5.43
367	389	0.9	12008	205.8	0.14	7.3	3.4	158.3	0.22	1.69
138	146	0.6	1746	5.7	0.06	358.1	6.1	70.7	0.43	7.69
208	217	0.3	3778	33.0	0.02	9.5	3.8	59.5	0.16	1.72

[1] L: length of bedding trace (m)
[2] R: maximum residual to plane (m)

Table 3: Summary of notation

Symbol	Meaning	
i	In subscript, represents component of 3D vector basis in 1-3	
n	Number of samples in data matrix	
$*$	In subscript, represents all n samples in data matrix.	
$\mathbf{x}$, x_i	Orthonormal basis vectors defining "world" coordinates	3×1
$\mathbf{D}$	Data matrix in "world" coordinates	$n \times 3$
$\boldsymbol{\mu}_{\mathbf{D}}$	Column-wise mean of data matrix	
Principal component analysis		
$\mathbf{M}$	Data matrix centered on all axes	$\mathbf{M} = \mathbf{D} - \mu_{\mathbf{D}}$
$\mathbf{C}$	Data covariance matrix for $\mathbf{M}$	$\mathbf{C}(n-1) = \mathbf{M}^{\mathrm{T}}\mathbf{M}$
$\boldsymbol{\lambda}$, λ_i	Vector of eigenvalues of $\mathbf{M}$	
$\boldsymbol{\Lambda}$	Diagonal matrix of eigenvalues of $\mathbf{M}$	$\boldsymbol{\Lambda} = \mathbf{I}\,\boldsymbol{\lambda}$
$\mathbf{V}$	Rotation matrix of orthonormal eigenvectors	3×3
$\mathbf{v}_i$	Eigenvector rows making up $\mathbf{V}$	
$\mathbf{n}$	Normal vector to the best-fitting plane	$\mathbf{n} = \mathbf{v}_3$
$\overline{\mathbf{x}}$, $\overline{\mathrm{x}}_i$	Orthonormal coordinate basis aligned with principal component axes $\mathbf{v}_i$	
$\overline{\mathbf{M}}$	Data matrix aligned with principal component axes	$\overline{\mathbf{M}} = \mathbf{M}\,\mathbf{V}^{\mathrm{T}}$
Singular value decomposition		
$\mathbf{U}$	Left singular vectors of $\mathbf{M}$	$n \times 3$
$\mathbf{S}$	Diagonal matrix of the singular values of $\mathbf{M}$	eigenvalues of $\mathbf{C}$
$\mathbf{s}$, s_i	Vector of singular values	$\mathbf{s} = \sqrt{\boldsymbol{\lambda}\,(n-1)}$
Statistical error analysis		
$\sigma_{\overline{\mathbf{M}}}$	Standard error of data matrix	$\sigma_{\overline{\mathbf{M}}} = \sqrt{\boldsymbol{\lambda}} = \frac{\mathbf{s}}{\sqrt{n-1}}$
$\sigma_{\boldsymbol{\lambda}}$	Standard error of the estimator	
d	Degrees of freedom of the estimator	$d = 2$ for angular error analysis
α	Confidence level for an error surface	$\alpha = 0.95$ is typical
$F_{\alpha,d,n-d}$	Fisher percent-point test statistic	
Construction of error surfaces		
$\mathbf{p}$	Parameters of the nominal plane in $\overline{\mathbf{x}}$	$\mathbf{p} = \boldsymbol{\lambda}$
$\mathbf{e}$	Errors to the nominal plane in $\overline{\mathbf{x}}$	$\mathbf{e} = F_{\alpha,d,n-d}\sigma_{\boldsymbol{\lambda}}$
$\mathbf{h}$	Semimajor axes of hyperbolic quadric defining an error surface	$\mathbf{h} = \mathbf{p} + \mathbf{e}$
$\mathbf{Q}$	5×5 matrix representation of a quadric surface	*as defined in text*
$\overline{\mathbf{Q}}_{\mathbf{H}}$	Tensor representation of a hyperbolic error quadric for semiaxes $\mathbf{h}$	
$\mathbf{T}$	An affine or projective transformation matrix	*as defined in text*
$\mathbf{C}$	4×4 matrix representation of conic section	*as defined in text*
Spherical errors		
γ	Angle in $[0, 2\pi]$ from $\overline{\mathrm{x}}_1$ within $\overline{\mathrm{x}}_{1,2}$ plane	
$\overline{\mathbf{x}}_\gamma$	2D coordinate basis orthogonal to nominal plane, defined by $\overline{\mathrm{x}}_\gamma, \overline{\mathrm{x}}_3$	
θ_γ	Angular error for an arbitrary direction within the plane	
θ_{max}, θ_{min}	Maximum and minimum angular errors at $\gamma_{\text{min}} = 0, \gamma_{\text{max}} = \frac{\pi}{2}$	

3.2.2 Finding principal components The original data matrix $\mathbf{D}$ is a $n \times 3$ matrix containing three-axis coordinates in a Cartesian coordinate system (commonly 3D geographical points in UTM or another local geodetic system). The centered data matrix $\mathbf{M}$ is centered

$$\mathbf{M} = \mathbf{D} - \boldsymbol{\mu}_{\mathbf{D}} \tag{1}$$

by subtraction of the mean along each axis.

PCA is formally described as an eigenvector decomposition of the sample covariance matrix $\mathbf{C}$, where

$$\mathbf{C} = \frac{1}{n-1}\mathbf{M}^{\mathrm{T}}\mathbf{M}, \tag{2}$$

the cross-product matrix of $\mathbf{M}$ scaled by the number of independent observations in the dataset. For our centered data, the decomposition is shown as

$$\mathbf{C} = \mathbf{V}\boldsymbol{\Lambda}\mathbf{V}^{\mathrm{T}} \tag{3}$$

where $\mathbf{V}$ is a rotation matrix composed of the eigenvectors and $\boldsymbol{\Lambda} = \boldsymbol{\lambda}\mathbf{I}$ is the diagonal matrix of eigenvalues of $\mathbf{C}$. These eigenvalues represent the variance of $\mathbf{M}$ along each eigenvector row of $\mathbf{V}$, denoted as $\mathbf{v}_i$.

Singular value decomposition, a more numerically stable technique to find the eigenvector decomposition of $\mathbf{C}$, is represented as

$$\mathbf{U}\,\mathbf{S}\,\mathbf{V}^{\mathrm{T}} = \mathbf{M}, \tag{4}$$

where $\mathbf{U}^{\mathrm{T}}\mathbf{U} = \mathbf{V}^{\mathrm{T}}\mathbf{V} = \mathbf{I}$ and $\mathbf{S}$ is a diagonal matrix of the singular values of the data matrix $\mathbf{M}$. The singular values are directly proportional to the eigenvalues of the data covariance matrix: $\boldsymbol{\Lambda} = \frac{1}{n-1}\mathbf{S}^2$. Expressed in scalar terms with $\mathbf{s} = \mathrm{trace}\,(\mathbf{S})$, this is equivalent to

$$\boldsymbol{\lambda} = \frac{\mathbf{s}^2}{n-1}. \tag{5}$$

3.2.3 Rotation into a principal-component aligned frame Geometrically, PCA corresponds to rotation of the dataset into a decorrelated reference frame. The rotation matrix $\mathbf{V}$ operates on the covariance matrix $\mathbf{C}$ to eliminate cross-correlations between components, defining a new coordinate basis aligned with the directions of maximum variability of the dataset. This rotated orthonormal coordinate basis, $\overline{\mathbf{x}}$, is aligned with the axes of $\mathbf{V}$ [Figure 1]. An arbitrary vector $\mathbf{a}$ in the global Cartesian plane can be rotated into this coordinate system using $\overline{\mathbf{a}} = \mathbf{a}\,\mathbf{V}^{\mathrm{T}}$.

Rotation of data into a principal-component aligned coordinate basis significantly eases error analysis and visualization of the structure of the dataset relative to its best-fitting plane. The "axis-aligned" projection of the input dataset $\overline{\mathbf{M}}$, defined as $\overline{\mathbf{M}} = \mathbf{M}\mathbf{V}^{\mathrm{T}}$, collapses the dataset

onto its best-fitting plane. Inverting Equation 3, the sample covariance matrix $\mathbf{C}$ can be expressed in this coordinate system as

$$\overline{\mathbf{C}} = \mathbf{\Lambda} = \boldsymbol{\lambda}\mathbf{I} = \mathbf{V}^{\mathrm{T}}\mathbf{C}\mathbf{V}. \tag{6}$$

The rotated dataset $\overline{\mathbf{M}}$ varies independently along each axis of $\overline{\mathbf{x}}$, and the magnitude of the eigenvalues $\boldsymbol{\lambda}$ of the PCA fit is proportional to the scale of the dataset along each principal component axis. The eigenvalues are equivalent to the three-component vector variance of the decorrelated data along each axis of $\overline{\mathbf{x}}$:

$$\boldsymbol{\lambda} = \boldsymbol{\sigma}^2_{\overline{\mathbf{M}}}. \tag{7}$$

The axes $\overline{\mathbf{x}}_1$ and $\overline{\mathbf{x}}_2$ fall within the best-fitting plane through the dataset, and $\overline{\mathbf{x}}_3$ is along the normal to the plane. Scatter along this axis represents the error in the planar fit. Thus, the third column of the aligned data matrix, $\overline{\mathbf{M}}_{*,3}$, represents residuals from the nominal planar fit. Rotation of the dataset into $\overline{\mathbf{x}}$ provides a useful means to understand the distribution of residuals and potential nonrandom structure relative to the best-fitting plane. Plotting $\overline{\mathbf{M}}_{*,1}$ vs. $\overline{\mathbf{M}}_{*,2}$ yields a plan view of the dataset, and $\overline{\mathbf{M}}_{*,i}$ vs. $\overline{\mathbf{M}}_{*,3}$ for $i = 1, 2$ shows residuals [Figure 5].

3.2.4 Strike and dip of the nominal plane The first and second eigenvector rows of $\mathbf{V}$ describe the planar fit in the absence of errors. The third eigenvector row of $\mathbf{V}$ is orthogonal to the plane; this normal vector $\mathbf{n} = \mathbf{v}_3$ can be used with the mean of the dataset $\boldsymbol{\mu}_{\mathbf{D}}$ (which the regression passes through by definition), to form an equation for the plane

$$\mathbf{n}\,\mathbf{X} + \mathbf{n} \cdot \boldsymbol{\mu}_{\mathbf{D}} = 0, \tag{8}$$

where $\mathbf{X}$ is a set of points within the plane. The nominal strike and dip in a geographic framework (*strike* defined relative to north) are calculated as follows:

$$(\mathit{strike}, \mathit{dip}) = \left(\tan^{-1} \frac{\mathrm{n}_1}{\mathrm{n}_2} - \frac{\pi}{2},\ \cos^{-1} \frac{\mathrm{n}_3}{\|\mathbf{n}\|} \right) \tag{9}$$

3.3 Confidence intervals for planar orientations

Errors to a planar measurements arise from statistical uncertainties on the parameters of a planar fit, and accurate modeling of errors requires the incorporation of a statistical distribution that is responsive to variation in input data quality. Given the formal relationship between PCA and OLS, we show that λ can be treated analogously to the OLS fit parameters $\hat{\beta}$ to define the error space to the plane, which can be represented as a hyperbolic error shell $\mathbf{h}$. Dataset orientation errors are scaled by the Fisher (F) statistical distribution to produce standardized orientation errors.

3.3.1 Eigenvectors as regression parameters The statistical basis for PCA regression errors can be developed from the widely-used OLS regression. The closed-form equation for OLS is given by

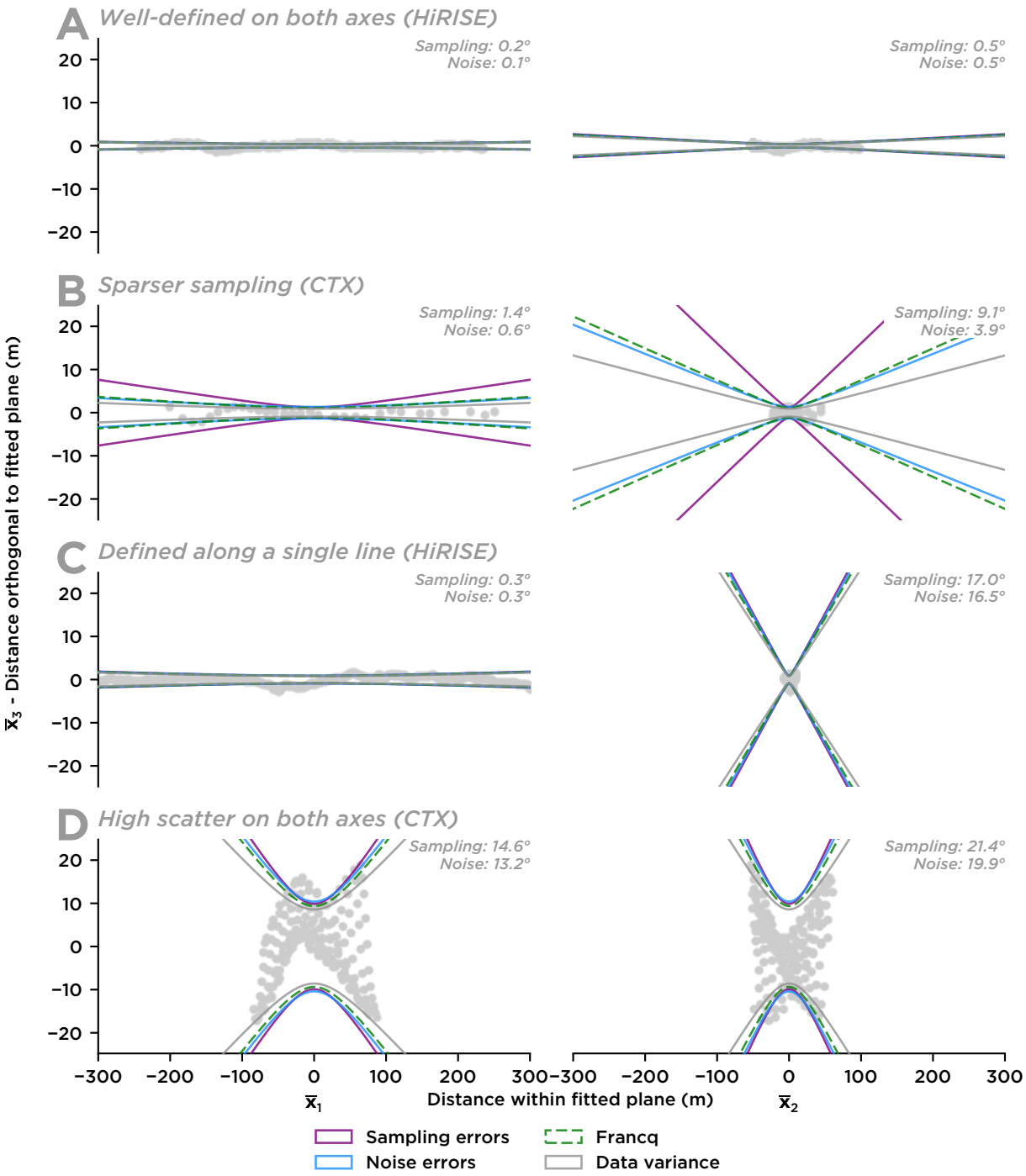

Figure 5: The Cartesian error space of fitted orientation measurements corresponding to example bedding traces [Figure 4]. Each plane is decomposed into two views aligned with $\overline{\mathbf{x}}$, with in-plane variation shown on the horizontal axis and out-of-plane variation on the vertical. The data making up the planar measurement is shown as grey points, and hyperbolic error bounds computed by several methods are overlain. Angular errors are not to scale. Each fitted plane has a distinct error structure depending on the characteristics of the input point cloud. **(a)** A well-fitted plane with low errors on all axes. **(b)** A slightly poorer fit with minimal definition along $\overline{\mathbf{x}}_2$. **(c)** A plane well-defined along $\overline{\mathbf{x}}_1$ but essentially undefined along $\overline{\mathbf{x}}_2$. **(d)** A fit poorly defined on both axes.

$$\hat{\beta}_{\text{OLS}} = (\mathbf{X}^{\text{T}}\mathbf{X})^{-1}\mathbf{X}^{\text{T}}\mathbf{y} \tag{10}$$

where $\mathbf{X}$ is a matrix of explanatory variables (a $n \times 2$ matrix for 3D data), and $\mathbf{y}$ is a column vector of dependent variables. Errors to the regression coefficients $\hat{\beta}$ can be estimated using the variance of these parameters.

$$\text{var}\left(\hat{\beta}_{\text{OLS}}\right) = \sigma^2(\mathbf{X}^{\text{T}}\mathbf{X})^{-1}, \tag{11}$$

where σ^2 is the mean squared error of the residuals to the fit.

Expressing the result of the PCA transformation in $\overline{\mathbf{x}}$ creates a degenerate case which is directly comparable to OLS and allows an equivalent construction of fit errors. Errors to PCA are by definition oriented along $\overline{\mathbf{x}}_3$, aligned with the vertical uniaxial errors assumed by OLS. In this framework, the regression parameters $\hat{\beta}$ can be recast as orthogonal slopes aligned with x_1 and x_2. The inputs to PCA can also be modified to conform to the notation used OLS: for a mean-centered point cloud, $\mathbf{M} = [\mathbf{X}\,\mathbf{y}]$, and the components of the fit can be represented as subspaces of the covariance matrix [Equation 2], where n is the number of data points:

$$\mathbf{C}(n-1) = \mathbf{M}^{\text{T}}\mathbf{M} = \begin{bmatrix} \mathbf{X}^{\text{T}}\mathbf{X} & \mathbf{X}^{\text{T}}\mathbf{y} \\ \mathbf{y}^{\text{T}}\mathbf{X} & \mathbf{y}^{\text{T}}\mathbf{y} \end{bmatrix}_{3\times 3}. \tag{12}$$

In aligned coordinates, $\overline{\mathbf{M}}^{\text{T}}\overline{\mathbf{M}} = \mathbf{\Lambda}(n-1)$; since $\mathbf{\Lambda}$ is a diagonal matrix, $\mathbf{X}^{\text{T}}\mathbf{y}$ reduces to $[0,0]^{\text{T}}$ because it is off the diagonal. In $\overline{\mathbf{x}}$ aligned with the PCA fit, the regression parameters $\hat{\beta}_{\text{PCA}} = [0,0]$ by definition. However, the variance of these parameters can illuminate the error structure to the planar fit. The variance of the regression parameters var $\left(\hat{\beta}_{\text{PCA}}\right)$ can be modeled by substitution for $\mathbf{X}^{\text{T}}\mathbf{X}$, yielding

$$\text{var}\left(\hat{\beta}_{\text{PCA}}\right) = \sigma^2 \begin{bmatrix} \lambda_1(n-1) & 0 \\ 0 & \lambda_2(n-1) \end{bmatrix}^{-1}. \tag{13}$$

Substituting $\sigma^2 = \lambda_3$, this reduces to

$$\text{var}\,\hat{\beta} = \begin{bmatrix} \frac{\lambda_3}{\lambda_1} & \frac{\lambda_3}{\lambda_2} \end{bmatrix}. \tag{14}$$

Even though "regression parameters" are a poor conceptual fit for PCA, regression errors are equivalent to a ratio of PCA eigenvalues.

This parallel can be extended to the statistical definition of errors. In OLS, var $\hat{\beta}$ captures regression errors specific to the sample measured. This "sample parameter" is a maximum-likelihood estimator of the errors to the true population fit parameter, var β, which can be parameterized as

$\text{var}\,\hat{\beta} + \text{error}\left(\text{var}\,\hat{\beta}\right)$ (*Fahrmeir et al.*, 2013). This error adds a statistical distribution to abstract the sample size and degrees of freedom in the input dataset, creating errors that can be compared between measurements.

For PCA, the eigenvalues λ_i that represent the dataset are equivalent to the sample variance of the dataset along each major axis [Equation 7], and the population variance along each axis is equivalent to $\lambda_i + \text{error}\,(\text{var}\,\lambda_i)$. Since PCA eigenvectors are orthogonal, their eigenvectors are statistically independent (*Jolliffe*, 2002, p. 46) and can be straightforwardly ratioed. Extending Equation 14, statistical errors to the planar estimator can be expressed as a ratio of uncertain eigenvalues:

$$\text{var}\,\beta_{\text{PCA}} = \left[\frac{\lambda_3+\text{error}(\lambda_3)}{\lambda_1+\text{error}(\lambda_1)} \quad \frac{\lambda_3+\text{error}(\lambda_3)}{\lambda_2+\text{error}(\lambda_2)}\right]. \tag{15}$$

Although errors parameterized as slopes are directly comparable to OLS errors, the orthogonality of PCA allows the direct representation of regression error as a hyperbolic surface [Figure 2], which can be manipulated with vector and tensor algebra, increasing flexibility for data visualization [Section 3.4]. The two orthogonal slopes that make up $\text{var}\,\beta_{\text{PCA}}$ are equivalent to tangents to an elliptic hyperboloid on two orthogonal axes aligned with the PCA fit. This error hyperboloid has semimajor axes defined by

$$\mathbf{h} = \boldsymbol{\lambda} + \text{error}\,(\boldsymbol{\lambda})\,. \tag{16}$$

This equation can also be parameterized as

$$\mathbf{h} = \mathbf{p} \pm \mathbf{e}, \tag{17}$$

with $\mathbf{p} = \boldsymbol{\lambda}$ representing the nominal plane parameters and $\mathbf{e} = \text{error}\,(\boldsymbol{\lambda})$ representing errors to each eigenvalue. $\mathbf{p}$, $\mathbf{e}$, and $\mathbf{h}$ are vectors with components along each axis in $\overline{\mathbf{x}}$. Below, we discuss formulations $\mathbf{p}$ and $\mathbf{e}$ used to construct the hyperbolic axes $\mathbf{h}$.

3.3.2 Regression error limited by data variance All regression fits must pass through the mean of the dataset, but the statistical definition of the central limit has important implications for the structure of planar orientation errors. The equivalence asserted between OLS variance and λ_3 [Equation 14] and carried through our definition of $\mathbf{p} = \boldsymbol{\lambda}$ [Equation 17] departs from standard regression statistics, with major effects on the modeled error structure of planes.

In standard regression statistics, the best-fitting plane is modeled as passing through the *mean* of the dataset, which is known with more precision as sample size increases. This "mean-limited" construction is tailored to modeling potential correlations between variables.

For fitting geological planes, all data points should be treated as estimates of the *true value* of a single plane. In this formulation of regression error, a high-quality fitted plane is defined by low variance, rather than well-known variance. This "variance-limited" framework explicitly models departures from a single plane, rather than the strength of correlations between scattered data.

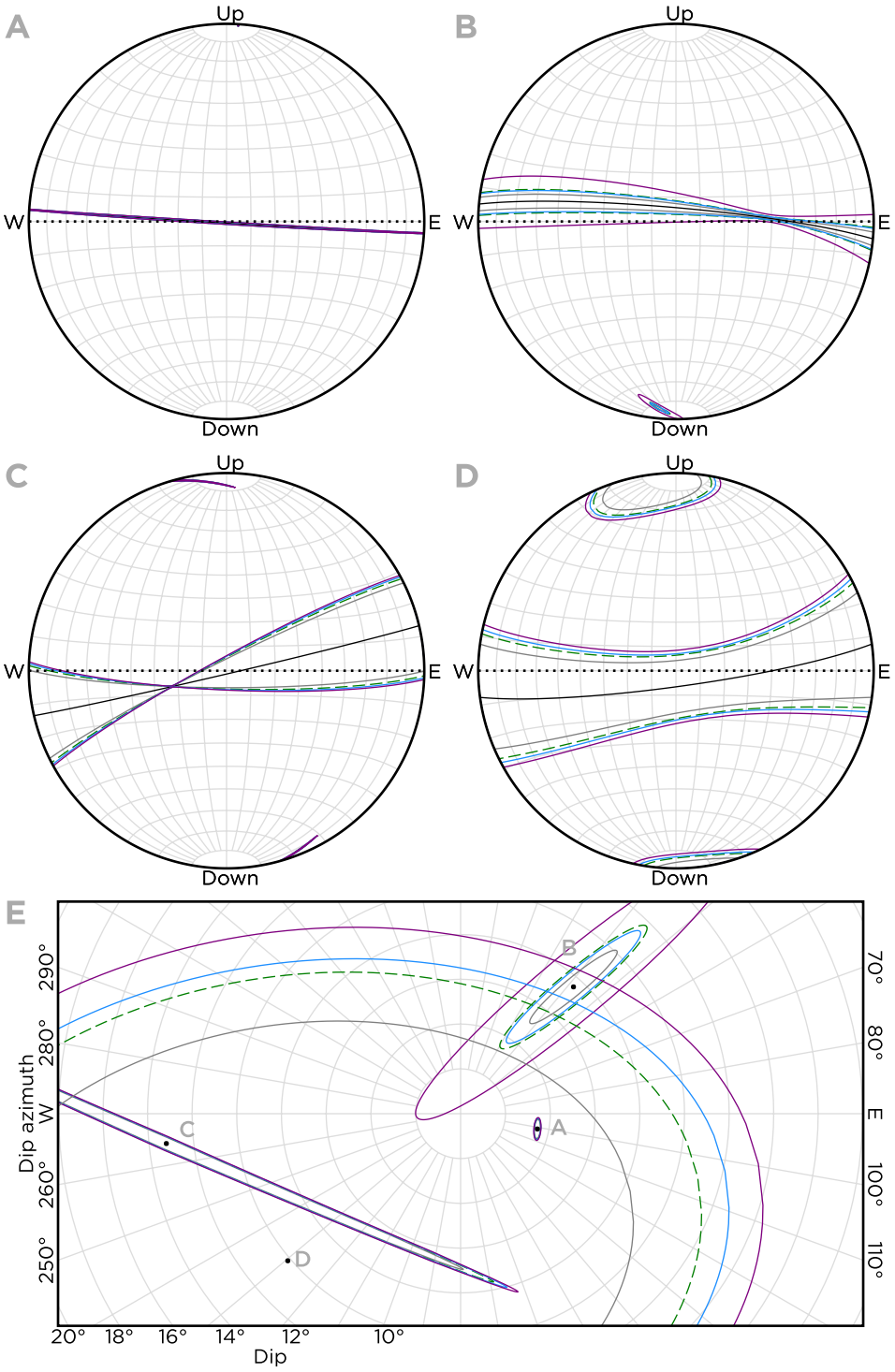

Figure 6: Projection of the hyperbolic errors to the plane into spherical coordinates to show angular errors. Estimates by different methods for computing **h** are colored as in Figure 5. **(a-d)** Spherical error space for each of the planes shown in Figure 5, projected onto oblique upper-hemisphere, equal area stereonets. **(e)** Error space to the bedding pole for each of the planes in panels *a-d*.

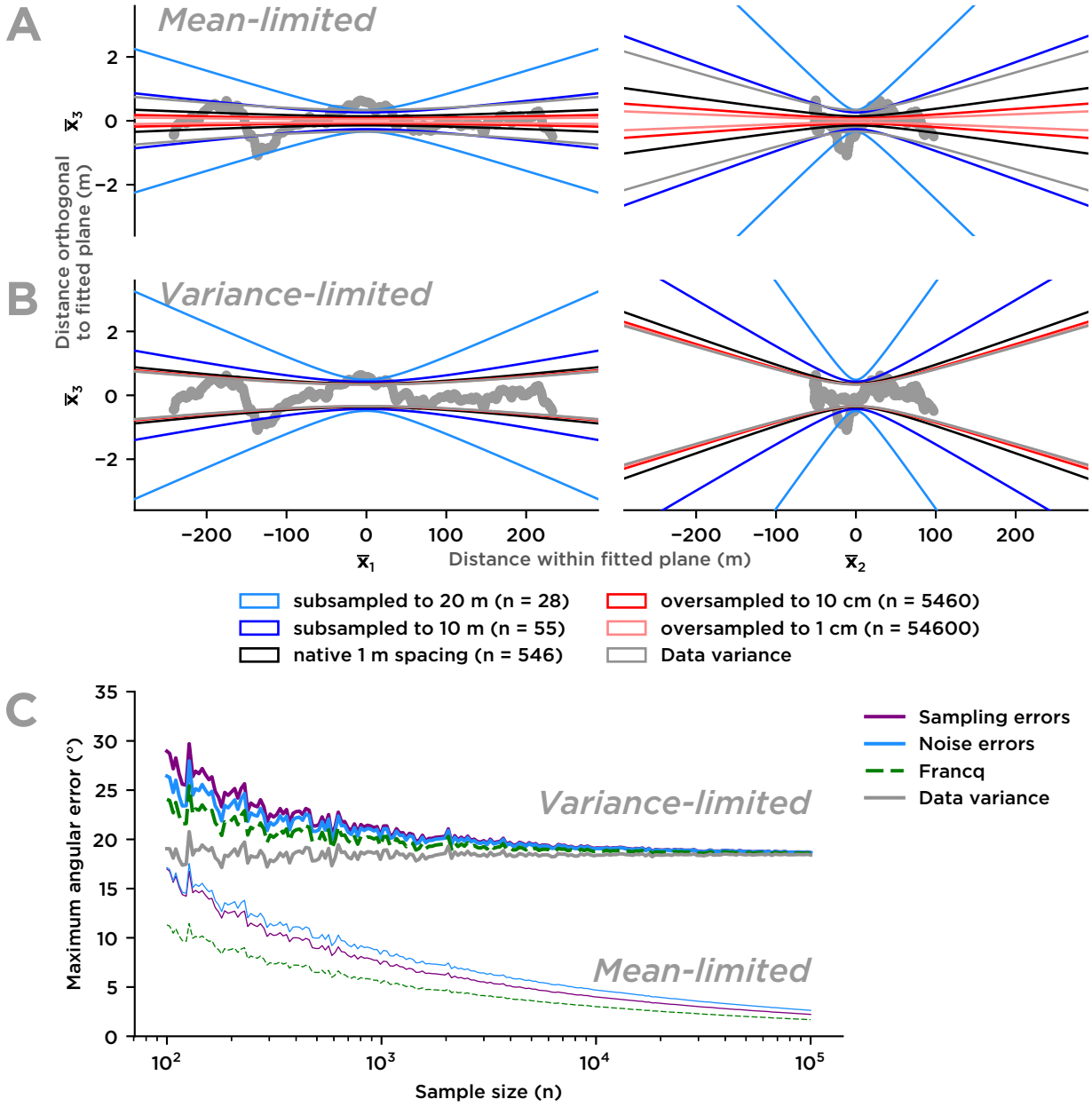

Figure 7: Exploration of centroid behavior with sample size. **(a)** Standard regression statistics applied to the "noise variance" method, with errors scaled to the quality of estimate of the mean. **(b)** Variance-limited regression modeling all points as estimates of a single true plane. This procedure is more resistant to dependence of error scaling on sample size. **(c)** Exploration of variance with sample size for a randomly generated plane with axial lengths $\mathbf{h} = [100, 10, 5]$, using several methods for variance estimation. All methods have errors that trend to 0 at large sample sizes when the dataset centroid is estimated by the mean.

The definition of the dataset centroid significantly alters the error structure on the out-of-plane axis $\overline{\mathbf{x}}_3$. For mean-limited scaling, λ_3 is not considered a regression error, and $\mathbf{p} = [\lambda_1,\ \lambda_2,\ 0]$. Since the standard error of the mean of a dataset is equivalent to the error of the variance, error (λ_3) represents the out-of-plane error and $\mathbf{e}$ is equivalent in both frameworks.

Mean-limited statistics significantly underestimate angular certainty in cases with large sample sizes [Figure 7a], complicating comparisons of measurements with different sampling characteristics. This is particularly relevant to fitting geologic planes, because spatial data from sensors can be at different spatial resolutions, or smoothed in a fashion that boosts sampling without changing the fundamental error structure.

In variance-limited statistics, data variance along $\overline{\mathbf{x}}_3$ sets a floor for errors to the plane. This parameterization of errors penalizes large departures from an idealized plane and preserves the basic structure of angular errors regardless of data density [Figure 7b]. This feature is crucial for comparing planes with different sampling characteristics. Most "off-the-shelf" packages for planar fitting use standard mean-centered statistics, suggesting that measurements made using these packages may be fundamentally biased by sample size effects.

3.3.3 Errors to eigenvectors To move from the decomposed variance of the dataset exposed by PCA to a statistically-based error distribution around a planar fit, we define $\mathbf{e}$ in terms of the certainty of the eigenvalues as such:

$$\mathbf{e} = \text{error}\,(\boldsymbol{\lambda}) = F_{\alpha,d,n-d}\,\sigma_{\boldsymbol{\lambda}}, \tag{18}$$

where F is the Fisher distribution statistic for $\alpha = 0.95$, $d = 2$, and the number of samples in the dataset (n). The statistical distribution incorporates the number of samples in the dataset (n) and the degrees of freedom of the statistical transformation (d). Several choices exist for the definition of $\sigma_{\boldsymbol{\lambda}}$, which we summarize below. Results for the four type cases are shown in Figure 5.

Data variance The most basic parametrization of orientation errors uses variance of the input dataset (i.e. eigenvalues) alone to represent the error space without $\sigma_{\boldsymbol{\lambda}}$, resulting simply in $\mathbf{h} = \mathbf{p} = \boldsymbol{\lambda}$. The data variance defines the basic structure of the plane, including its scaling based on out-of plane residuals [Section 3.3.2] and the directional dependence of fit quality. However, the lack of a statistical treatment of the accuracy of variance makes this method unresponsive to undersampling or differently-scaled datasets.

The data variance parameterization of orientation errors is developed in the paleomagnetism literature, where uncertain lines and planes model magnetometer response during laboratory measurements of rock remnant magnetism. These techniques treat the variance of the dataset (decomposed along its major axes by PCA) as a measure of fit quality for visualization and automated data-reduction pipelines (e.g. *Kirschvink*, 1980). This literature describes the parameterization of the PCA fit as an ellipsoid (the "dual" quadric to the hyperbola enclosing the plane; see

Appendix) with different potential shapes depending on dataset structure [Table 1, adapted from *Onstott* (1980)].

Sampling variance The simplest method of statistically-based error scaling uses multivariate statistics based on sample size. In this framework, errors assume that the measured data is a random sampling of a population that conforms to a Gaussian distribution. The expression for variance of the eigenvectors for PCA,

$$\sigma_{\boldsymbol{\lambda}}^2 = \frac{2\boldsymbol{\lambda}^2}{n-1}, \tag{19}$$

arises directly from the estimation of population variance in sampling statistics (*Jolliffe*, 2002, p. 48; *Faber et al.*, 1993).

Noise variance The standard assumption of Gaussian population statistics, that the variance of the sample is primarily a function of its size, may be imperfect when applied to continuously sampled data. Datasets that include all of the available data over an interval (i.e. aren't random samples of a population) are implicitly highly correlated. In this situation, sample-size based statistics may be misleading. Interpolated elevation data can easily be smoothed and overfitted, increasing apparent statistical power with little to no improvement in the quality of the fit. Conversely, when the noise in the input dataset is low, even small samples can show significant results. The noise variance framework for PCA errors (*Malinowski*, 1977; *Faber et al.*, 1993, 1995; *Faber and Kowalski*, 1997) is explicitly designed for use with continuously sampled data.

Instead of uniformly scaling errors along a given principal component axis $\overline{\mathbf{x}}_i$ with the singular values along that axis, noise covariance is based on the intuition that "measurement noise" defined along higher-dimensional axes provides a good estimate of the errors on all axes. In our case, scatter along $\overline{\mathbf{x}}_3$ is the "noise component" of the data, and may provide a better estimate of the scatter in $\overline{\mathbf{x}}_1$ and $\overline{\mathbf{x}}_2$ that the variance along these axes. Intuitively, the structure of the data cloud within the best-fitting plane is an artifact of digitization with no bearing on accuracy.

Faber et al. (1993) shows that the variance of the PCA eigenvectors can be modeled as

$$\sigma_{\boldsymbol{\lambda}}^2 = 4\,\boldsymbol{\lambda}\,\sigma_{\hat{\mathbf{M}}}^2, \tag{20}$$

where $\sigma_{\hat{\mathbf{M}}}^2$ is the "noise variance" of the data matrix. Methods to compute the noise variance $\sigma_{\hat{\mathbf{M}}}^2$ rely on the concept of "pseudorank", the rank of the aligned data matrix in the absence of noise. Detailed treatments of the noise variance framework (*Faber et al.*, 1995; *Faber and Kowalski*, 1997) discuss adjustment of the pseudorank to incorporate nonlinear bias, but this is unnecessary for our low-dimensional case. For three-dimensional data aligned along a plane, errors will be entirely contained in scatter on $\overline{\mathbf{x}}_3$. A plane without noise will be contained in the $\overline{\mathbf{x}}_1$–$\overline{\mathbf{x_2}}$ plane, with a pseudorank of $K = 2$.

Malinowski (1977) describes the "real error" component

$$\sigma^2_{\hat{\mathbf{M}}} = \frac{\sum_{p=K+1}^{c} \lambda_p}{r\,(c-K)} \tag{21}$$

where $r \times c$ is the dimensions of the data matrix $\mathbf{M}$. *Faber et al.* (1993) slightly modifies this to

$$\sigma^2_{\hat{\mathbf{M}}} = \frac{\sum_{p=K+1}^{c} \lambda_p}{(r-K)(c-K)} \tag{22}$$

based on experimental validation. For our purposes of planar fitting, $K = 2$, $r = n$, and $c = 3$, and these expressions collapse to $\sigma^2_{\hat{\mathbf{M}}} = \frac{\lambda_3}{n}$ (*Malinowski*, 1977) and $\sigma^2_{\hat{\mathbf{M}}} = \frac{\lambda_3}{n-2}$ (*Faber et al.*, 1993). With sample sizes $n \gg K$, the difference between these estimators is negligible. Combining Equation 20 with Equation 22, we can express the noise variance of the dataset as

$$\sigma^2_{\boldsymbol{\lambda}} = \frac{4\,\boldsymbol{\lambda}\,\lambda_3}{n-2}. \tag{23}$$

Other statistical distributions Several other treatments of errors given in the literature provide direct alternatives for scaling $\mathbf{e}$ with different statistical assumptions. *Francq and Govaerts* (2014) provides a formulation of error bars for two-axis OLS, which can be generalized to the PCA framework, yielding error axes

$$\mathbf{e} = \boldsymbol{\lambda}\sqrt{\frac{2}{n-2}F_{\alpha,d,n-d}}. \tag{24}$$

This formulation provides slightly more constrained errors than both sampling and noise-based errors, due to the co-dependence of errors of variables defined in global Cartesian coordinates. *Babamoradi et al.* (2013) provides an implementation that closely tracks the "sampling variance" method with slightly different scaling for sample sizes. *Weingarten et al.* (2004) describes a numerical method which applies OLS regression after PCA rotation, using the slope found by OLS in $\overline{\mathbf{x}}$ to estimate var β_{PCA}.

Choice of $\sigma_{\boldsymbol{\lambda}}$ or $\mathbf{e}$ The effect of using different test statistics is minimal for well-sampled data, and results asymptotically converge on the data variance at large sample sizes [Figure 5 and Figure 6]. The formulations tested show similar results, but the "noise error" is more resistant to changes in sample density [Figure 5c and d]. We use the noise error as the preferred scaling in software and graphical implementations of this method.

3.3.4 Statistical error scaling To create confidence intervals, we apply a Fisher $\left(F_{\alpha,d,n-d}\right)$ statistical distribution to $\sigma_{\boldsymbol{\lambda}}$ using Equation 18 with the $\sigma_{\boldsymbol{\lambda}}$ formulation in Equation 23. The eigen-

values of the dataset follow the $\chi^2_{\alpha,d}$ distribution. Since regression parameters are composed of ratios of eigenvalues [Equation 14], the appropriate test statistic for orientation data is the Fisher distribution, $F_{\alpha,d,n-d}$, which models ratios of χ^2-distributed parameters (*Jolliffe*, 2002; *Francq and Govaerts*, 2014; *Babamoradi et al.*, 2013). At large sample sizes, $lim_{n\to\infty} F_{\alpha,d,n-d} = \frac{1}{d}\chi^2_{\alpha,d}$. For planar orientations, $d = 2$, since the orientation information contained in the three eigenvectors can be summarized as two ratios. The remaining parameter, α, is the confidence level at which the distribution should be queried. For typical analysis, $\alpha = 0.95$, corresponding to a 95% confidence interval, should suffice.

The resulting parameterization of the errors to the eigenvectors is summarized as

$$\mathbf{e}_{\boldsymbol{\lambda}} = F_{\alpha,d,n-d}\boldsymbol{\sigma}_{\boldsymbol{\lambda}}. \tag{25}$$

Thus, for noise errors,

$$\mathbf{e}_{\boldsymbol{\lambda}} = F_{\alpha,d,n-d}\sqrt{\frac{2\boldsymbol{\lambda}}{n-2}}\lambda_3. \tag{26}$$

Since the dataset variance itself is a source of error, $\mathbf{e} = \lambda_3 + \mathbf{e}_{\boldsymbol{\lambda}}$. To construct the hyperbolic error space of the plane, we recall that $\mathbf{h} = \mathbf{p} \pm \mathbf{e}$ [Equation 17]. At any level of error, the maximum bounding surface of $\mathbf{h}$ occurs when the length of in-plane axes of the hyperboloid are minimized and out-of-plane error is maximized. Thus, the maximum error shell used for visualization is

$$\mathbf{h}_* = [\lambda_1 - \mathrm{e}_1,\ \lambda_2 - \mathrm{e}_2,\ \lambda_1 + \mathrm{e}_3], \tag{27}$$

or alternatively

$$\mathbf{h} = \boldsymbol{\lambda} + \mathbf{a}F_{\alpha,d,n-d}\boldsymbol{\sigma}_{\boldsymbol{\lambda}}, \tag{28}$$

where $\mathbf{a} = [-1, -1, 1]$ denotes whether errors are subtracted or added along that axis to form the maximum error surface.

3.4 Displaying orientation error surfaces

Armed with a statistical framework for the errors to planar measurements, we turn to methods to display these errors graphically in Cartesian and spherical coordinates, represented schematically in Figure 2. Projections of error bounds as 2D hyperbolic slices and spherical ellipses and girdles provide useful visualizations of the error structure of the plane. These visualization techniques rely only on the statistically derived hyperboloid with semiaxes $\mathbf{h}$ which represents the uncertain plane, independent of the statistical assumptions used in its construction. In principle, the mechanisms for plotting error distributions apply equivalently to planes regressed using OLS, but the orthogonality of PCA errors to the regression line results in simpler linear algebra. Generalized equations for quadric surfaces that can be manipulated with transformation matrices and quaternion rotations are discussed in the Appendix; here we focus on common cases used

to develop key visualizations of the error space.

3.4.1 Projection to hyperbolic errors Two-dimensional conic slices of the hyperbolic error space of the plane summarize dataset structure in PCA-aligned coordinates or projected into real space. Errors can assessed along any axis, but slices of the error hyperboloid aligned with the major axes of the planar fit are the most intuitive. These "axis-aligned" views of the dataset, with in-plane variation on the horizontal axis and out-of-plane variation on the vertical, are the ideal decomposition to assess the structure of a fitted dataset and verify the quality of the input data $\mathbf{D}$. Visual inspection of dataset quality in PCA-aligned coordinates [Figure 5] is an important quality check on measured orientations. The measurements shown in Figure 5b and d both show significant out-of-plane variation potentially related to both DEM errors and digitizing errors.

A hyperbola can by constructed for a two-dimensional slice of the error quadric, along a coordinate basis $\overline{\mathbf{x}}_\gamma = [\overline{\mathrm{x}}_\gamma, \overline{\mathrm{x}}_3]$ with axis $\overline{\mathrm{x}}_\gamma$ within the plane defined as a linear combination of $\overline{\mathrm{x}}_1$ and $\overline{\mathrm{x}}_2$ as

$$\overline{\mathrm{x}}_\gamma = \sqrt{\overline{\mathrm{x}}_1 \cos^2\gamma + \overline{\mathrm{x}}_2 \sin^2\gamma}, \tag{29}$$

where $\gamma = [0, 2\pi]$ is the angle from $\overline{\mathrm{x}}_1$ within the plane. In this set of coordinates, h_γ can be defined a major axis to the 2D conic,

$$\mathrm{h}_\gamma = \sqrt{\mathrm{h}_1 \cos^2\gamma + \mathrm{h}_2 \sin^2\gamma}, \tag{30}$$

the radius of an ellipse defined by major axes h_1 and h_2 within the best-fitting plane. The axis-aligned hyperbolic slice of the hyperbolic error quadric can be represented as

$$\mathbf{C} = \mathrm{diag}\left(\tfrac{1}{\mathrm{h}_\gamma^2}, -\tfrac{1}{\mathrm{h}_3^2}, 1\right). \tag{31}$$

For a slice of the plane oriented along $\frac{1}{\mathrm{h}_1^2}$, $\gamma = 0$ and $\mathbf{h}_\gamma = [\mathrm{h}_1, \mathrm{h}_3]$. For an axis-aligned and mean-centered conic, the hyperbolic error bounds in are given by the equivalent representations

$$\overline{\mathrm{x}}_3 = \pm \mathrm{h}_3 \cosh\left(\sinh^{-1}\left(\tfrac{\overline{\mathrm{x}}_\gamma}{\mathrm{h}_\gamma}\right)\right) = \pm \mathrm{h}_3 \sqrt{\left(\tfrac{\overline{\mathrm{x}}_\gamma}{\mathrm{h}_\gamma}\right)^2 + 1}. \tag{32}$$

These error bars can be plotted as-is (e.g. Figure 5) or shifted from $\overline{\mathbf{x}}_\gamma$ to $\mathbf{x}$ using scaling and rotation as necessary. We discuss this more general transformation in the Appendix.

3.4.2 Spherical representation of errors The discussion and display of orientation errors has thus far been carried out in a Cartesian reference frame, but it is useful to represent uncertain planar fits in an angular framework. This allows plotting on stereonets and direct comparison to other orientation data.

For our rotational construction, given any in-plane axis h_γ, the angular errors from the nom-

inal plane are defined by tangents to the hyperbolic error sheets,

$$\theta_\gamma = 2\tan^{-1}\left(\mathrm{h}_3/\mathrm{h}_\gamma\right), \tag{33}$$

the factor of 2 arising from combining errors for both the upper and lower sheets of the hyperboloid. Solving this for $\gamma = [0, 2\pi]$ yields a girdle of angular error magnitudes relative to the great circle defining the nominal plane. The resulting distribution is a graphical representation of angular errors for all directions of the planar fit [Figure 6].

The angular error surfaces for the normal vector fall 90° from those representing the plane, forming an elliptical error space encompassing poles to the plane. Normal vector errors can be can be computed by a similar process to that used to generate a hyperbolic girdle around the plane, using the inverse of the tangents.

$$\mathrm{a}_\gamma = \tan^{-1}\left(\mathrm{h}_\gamma/\mathrm{h}_3\right) \tag{34}$$

evaluated over $\gamma = [0, 2\pi]$ defines the angular dimension of an error ellipse in spherical coordinates, defined relative to $\overline{\mathbf{x}}_3$. This ellipse can be rotated into global coordinates using the rotation matrix $\mathbf{V}$. A more general solution is discussed in Section A.2.

3.4.3 Maximum and minimum angular errors The best numerical summary of errors to an orientation measurement are the maximum and minimum angular errors, which are defined orthogonal to the plane and aligned with the major axes of the best-fitting plane. This concept can be applied to statistically derived error surfaces as well, given a set of axial lengths calculated by one of the methods above. For the semiaxes $\mathbf{h}$ corresponding to errors at a particular level,

$$(\theta_{\max},\, \theta_{\min}) = \left(2\tan^{-1}\left(\mathrm{h}_3/\mathrm{h}_2\right),\, 2\tan^{-1}\left(\mathrm{h}_3/\mathrm{h}_1\right)\right) \tag{35}$$

provides the angular width of the error distribution aligned with the major axes of the dataset. This allows errors to be reported in angular space, though their statistical development is undertaken entirely in Cartesian space. Because of the nonlinearity associated with angular transformations, there is no natural correspondence between the dip direction of a best-fitting plane and the direction of $\theta_{\max}$. To form a full representation of the errors, we must also report the azimuth of the error axis within the plane. This *rake* angle [Table 2] is defined as the angle between the strike and $\theta_{\max}$ (which is oriented along $\overline{\mathbf{x}}_2$) , calculated as

$$\textit{rake} = \cos\left(\left(\mathbf{v}_3 \times \mathbf{z}\right) \cdot \mathbf{v}_2\right), \tag{36}$$

where $\mathbf{z} = [0, 0, 1]$ is a vertical vector.

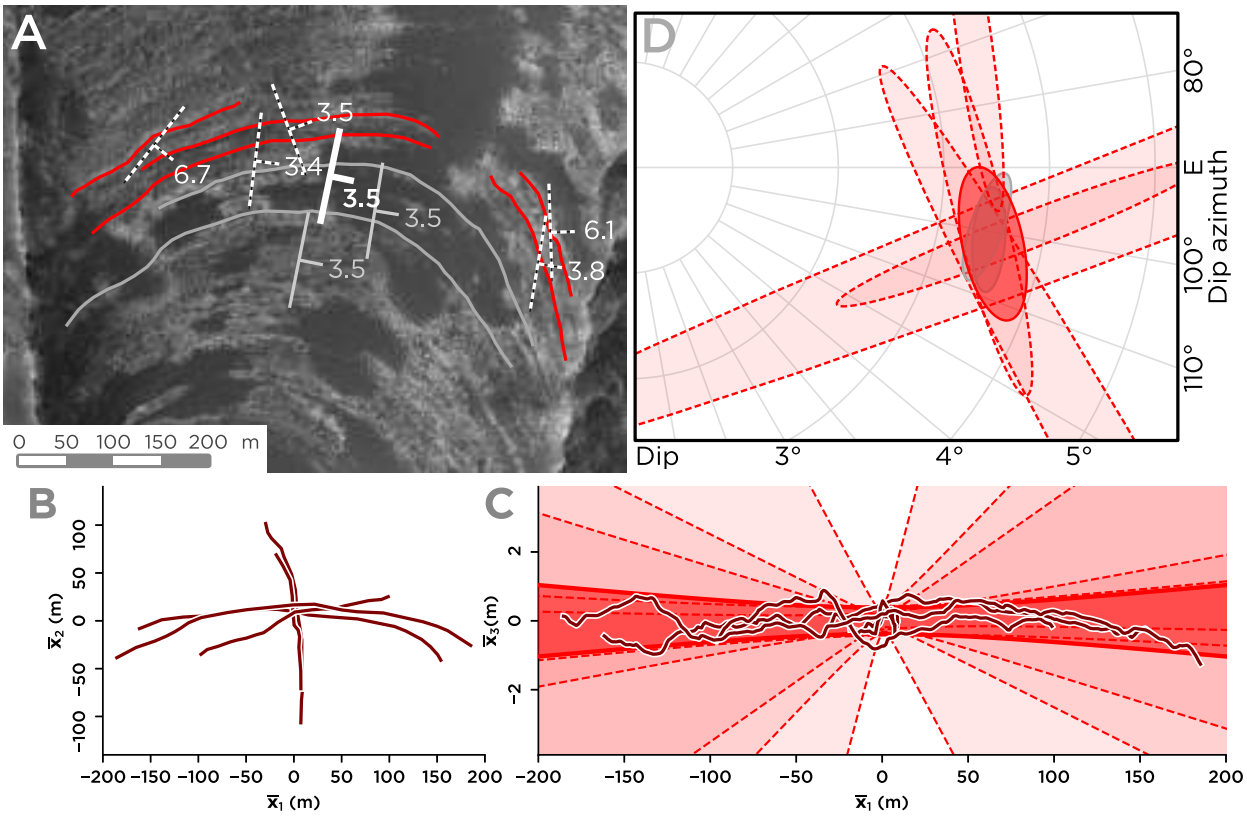

Figure 8: Joint fitting of bedding traces within a single stratigraphy to minimize errors for parallel planes. **(a)** Map view of bedding traces showing scattered nominal dips for bedding traces on opposing hillslopes (dashed), along with better-constrained orientations digitized around the entire range of hillslope aspect (solid bold). **(b)** Plan view of bedding traces centered and stacked atop each other for joint fitting, showing definition of a plane in two dimensions. **(c)** Side view of the plane showing residuals within the digitized dataset. Jagged lines are due to digitization errors. **(d)** Projection of errors to bedding poles on an upper-hemisphere stereonet, showing the grouped error range (red filled) at the intersection of the individual error spaces (dashed), and overlapping the error spaces of well-digitized single planes.

3.5 Joint fitting of parallel bedding planes

A common problem for remote sensing of geologically relevant areas is lack of continuous exposure, and planes that are unconstrained in one dimension are common [Figure 4]. However, exposures of bedding in close spatial association often capture slightly different cuts of topography with different orientation error structures. This is statistically useful: under the assumption of parallel bedding, multiple bedding traces can be jointly fitted to increase the three-dimensional definition of a planar dataset. Error metrics computed after fitting can be used to test the validity of this assumption.

In Figure 8, several bedding traces digitized on opposing hillslopes in the same cuesta show different error structures. Bedding traces that could be followed around the entire range of hillslope aspect have much more restricted error spaces. Grouping of the low-quality planar fits cre-

ates a much higher-precision joint measurement at the intersection of the error spaces of individual beds, showing nearly the same orientation as high-precision single-bed measurements.

The process of joint fitting is nearly the same as the single-plane fitting procedure outlined in Section 3.2 and Section 3.3. The only difference is in processing of the input data: prior to PCA regression, the data matrix $\mathbf{D}$ corresponding to each input point cloud is independently centered on its mean using Equation 1. The resulting matrices are stacked to form a single centered data matrix $\mathbf{M}$. This combined representation contains orientation info for each bedding traces, but discards information on the relative locations of the planes. The orientation of the combined data matrix is regressed using PCA and error is modeled using standard techniques. If the assumption of a shared bedding orientation is valid, this can vastly increase statistical power.

This technique removes the need for certainty in the bed-to-bed correspondence of adjacent but discontinuous stratigraphic exposures, which is often difficult to determine. However, the method must be applied with care: it is only valid where the assumption of parallel bedding holds. For this reason, the combination of this method with views of decomposed variance and statistical error bounds is particularly powerful. Evaluation of misfits from the joint plane can illuminate whether the assumption of shared stratigraphy is valid. If a grouping cannot be adequately modeled as a parallel stratigraphy, this will be clear from the input data. Joint fitting of planes can be valuable both for precise statistical modeling of parallel-bedded stratigraphies and as an exploratory tool to evaluate whether stratigraphies conform to a parallel-bedding assumption.

4 Method demonstration and performance

4.1 Orbital imagery of the San Rafael Swell, Utah

The San Rafael Swell in eastern Utah, USA, is a ~20×40 km Paleocene Laramide anticline formed above a west-dipping thrust fault in the subsurface that tilted the strata to nearly vertical, creating the imposing San Rafael "Reef" [Figure 9a]. This structure is cored by a Jurassic stratigraphy including the distinctive, thick aeolian Navajo sandstone (*Gilluly and Reeside Jr*, 1928). In the middle of the swell, these strata are eroded away. The dramatic transect of Interstate 70 across the center of the structure makes the San Rafael Swell a world-famous structural locale. At the eastern edge of the swell, east dips steepen from near-flat to a maximum of ~60° before shallowing outside of the reef [Figure 9b]. The simple fold pattern and well-exposed stratigraphic layering provide an ideal setting to test the recovery of orientation errors from orbital or airborne data, allowing orientation recovery to be tested at a wide range of dips against data collected *in-situ*.

4.1.1 Datasets The map database accompanying the recently published geologic map of the San Rafael Desert (*Doelling et al.*, 2017) provides bedding orientations from the structural map, which were measured in the field at outcrop scale using a compass clinometer. At regional scale, they outline the convex structure and N-S axis of the swell [Figure 9c]

A 5 m ground-sample distance DEM from the Utah Automated Geographic Reference Center

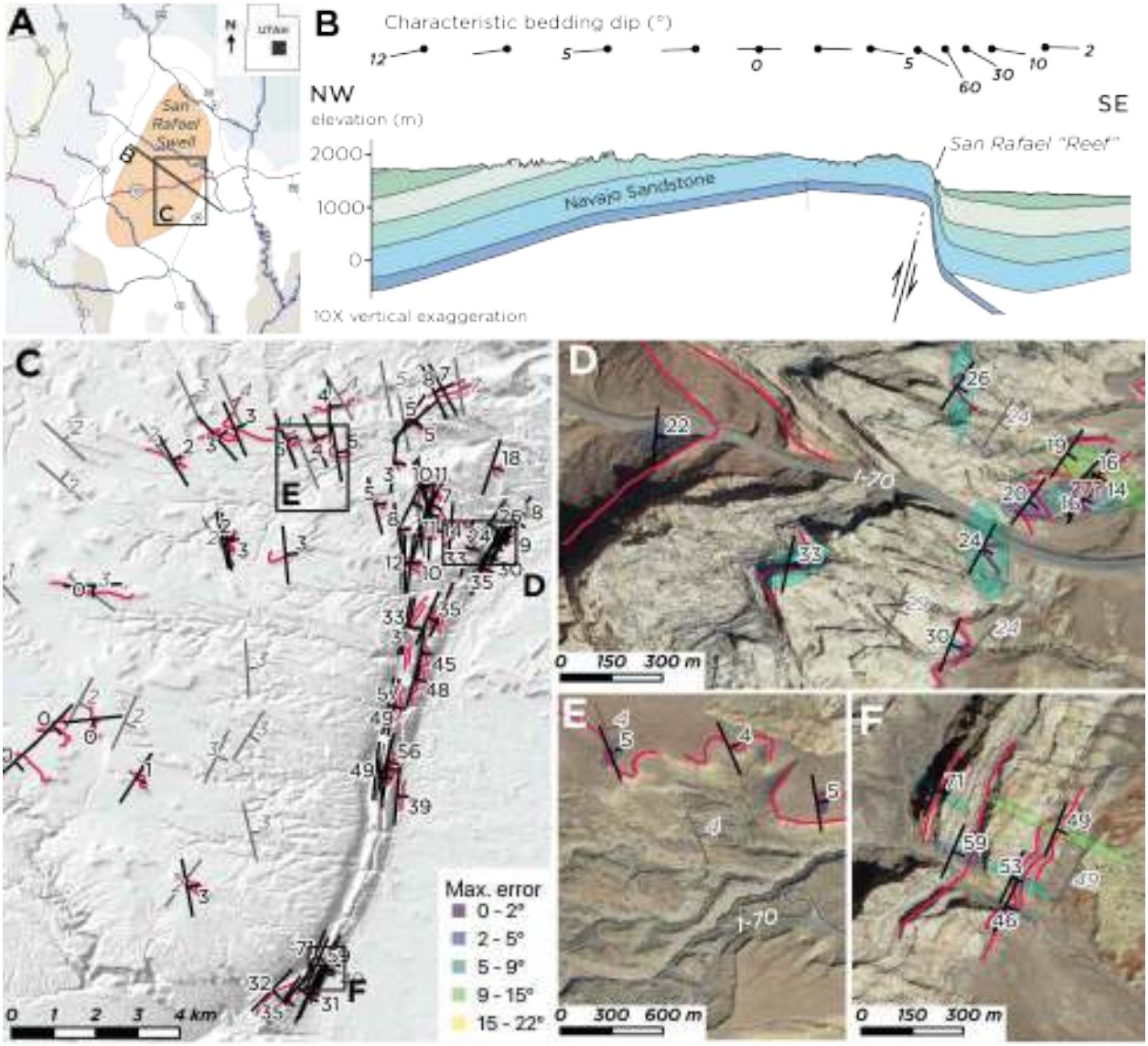

Figure 9: **(a)** Physiographic context of the San Rafael Swell in southeast Utah, USA. **(b)** Cross-section of the San Rafael Swell anticline (after *Doelling et al.*, 2017) showing the asymmetric dips of strata across the structure. **(c)** Field-measured bedding orientations (grey numbered symbols) from the San Rafael Desert geologic map (*Doelling et al.*, 2017), nominal remotely-sensed bedding orientations (black numbered symbols), and corresponding digitized bedding traces (red lines) atop a hillshade of the of the 5m aerial photogrammetric DEM used as input data for orientation reconstruction. Field-measured and remotely-sensed bedding orientations follow the same structural pattern. **(d-f)** Digitized bedding traces, remotely-measured orientations and field orientations atop orthorectified, coregistered *Google Maps* satellite data (accessed Feb. 2018) for key areas. Remotely-sensed orientations are underlain by an error-ellipse with axial lengths corresponding to θ_{max} and θ_{min}, oriented along the maximum direction of error.

was used as the elevation layer for digitized bedding traces. This DEM was created from autocorrelated 1-meter resolution stereo aerial imagery, using the SOCET Set software package. Elevation contours and a shaded-relief map were generated from the DEM to inspect alignment and data fidelity. In general, the DEM is of high quality, with a few artifacts in high-slope regions on the eastern side of steep hillsides where shadows lead to poor correlations. Locally, the data is significantly higher fidelity than the 10-meter resolution National Elevation Dataset (*Gesch et al.*, 2014)

Orthorectified, mosaicked ~25 cm/px satellite imagery from Google Maps was used to digitize bedding traces atop the DEM. The satellite imagery had been warped over a somewhat lower-resolution DEM than used here, leading to registration errors of up to 5 meters between the DEM and imagery datasets. Areas with obvious mismatch were avoided for digitization of features.

Bedding traces were digitized atop the satellite imagery using QGIS. Outcrops were chosen to maximize the 3D structure of captured planes, and areas near field-measured observations were targeted for direct comparison. Lengths of bedding traces range from 100 to 2500 m (median length 415 m). The longest traces are in low-dipping strata in the western portion of the study area. Digitized bedding traces are shown in Figure 9c.

The `orienteer` software package (see Appendix) was used to conduct planar fitting and evaluate the resulting planes for quality. During elevation extraction, lines were subset at 5 meter intervals to fully query the DEM. Planes were examined visually and quantitatively after PCA fits as described above. Those with large residuals (typically > 10 m out-of-plane) were re-measured if the blunder was due to an obvious mis-digitization, or discarded [Figure 10]. Sixty-eight planes were retained. Since only planes with favorable exposure were measured, no data grouping of beds was required to increase statistical power.

4.1.2 Orbital and field data comparison Overall, the map pattern of remotely-measured orientations mimics the large-scale structural trend of steepening dips towards the eastern monocline of the swell [Figure 9c]. Dip magnitudes are very close to those measured in the field. The direction and magnitude of errors are summarized as ellipses on the dip symbols. For the shallowest bedding, errors are extremely low [Figure 9d], while for the steepest measurements, errors are almost entirely in the dip direction [Figure 9e]. Error magnitudes are small for low-dipping strata and increase substantially with steeper dips. This is intuitive as the effects of DEM errors, poor registration of imagery, and digitizing errors will increase in rugged topography.

Selected closely spaced in-situ and remotely sensed orientation measurements paired for direct comparison [Figure 11] show that remotely-sensed orientations typically closely match the in-situ measurements, typically within error. Mismatch of a few degrees, especially in strike, can be explained by actual localized variation in bed orientation or slight measurement errors either in remote or in-situ gathered data. One measurement pair, highlighted in red on Figure 11, has an unusually large dip error. This in-situ measurement, at the eastern margin of the swell im-

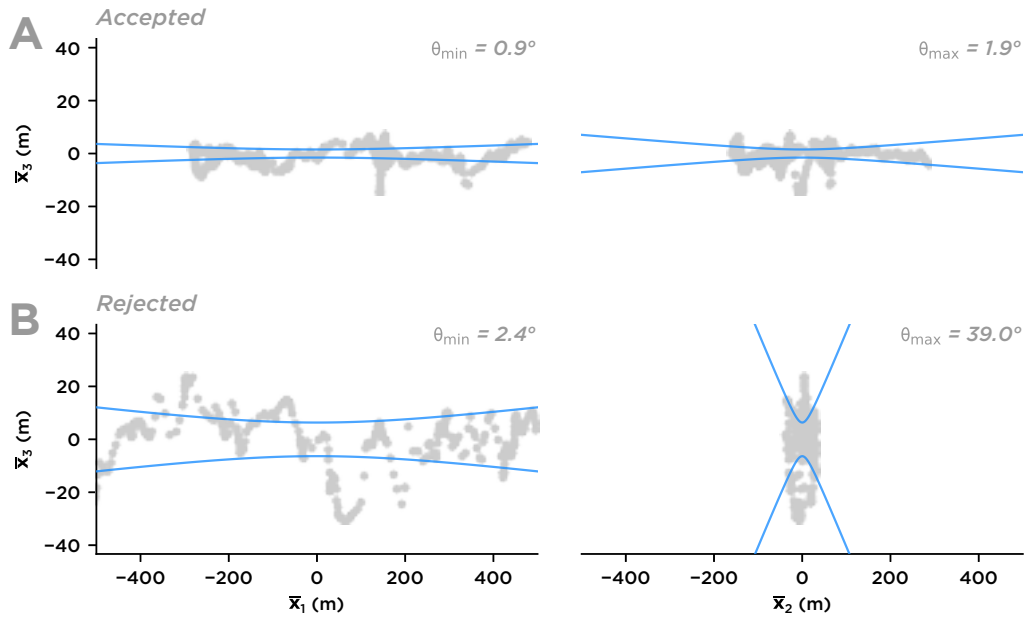

Figure 10: Axis-aligned visualization of fit errors to illustrate filtering criteria for poor bedding traces during creation of the San Rafael Swell dataset. **(a)** An accepted fit with relatively low out-of-plane scatter, defined over a significant length along both $\overline{\mathbf{x}}_1$ and $\overline{\mathbf{x}}_2$. **(b)** A poor fit, with higher out-of-plane scatter and no definition along $\overline{\mathbf{x}}_2$. This bedding trace was discarded from the dataset.

mediately north of the I-70 freeway, has a reported dip of 27°. We instead measure a dip, with error, of 10-20°. We replicate this result with additional measurements of several closely spaced beds. The 27° dip is steeper than those immediately westward, putting it at odds with the localized structural pattern of shallowing dips at the eastern edge of the swell. This suggests that the published dip measurement on this outcrop may be in error.

Although basic correspondence between the DEM and imagery was manually checked, no processing or alignment was applied to the input data. A higher level of processing might increase the fidelity of the digital surface model, but this example demonstrates that reasonable planar orientations can be extracted from minimally-processed, publicly available imagery datasets, especially when good exposure is available. The addition of error and its visualization to the analytical product enables much more flexibility in input data quality, as errors arising from poorly registered data or sloppy digitizing will be penalized by poor confidence metrics and readily recognized [e.g. Figure 10].

4.2 UAV photogrammetry in the Naukluft Mountains, Namibia

The eastern face of the Naukluft mountains adjacent to Onis Farm (24.32° S, 16.23° E) contains mixed siliciclastic and carbonate strata above a regionally significant thrust fault (*Rowe et al.*, 2012). Recent mapping and stratigraphic studies in the area identified a minimally deformed

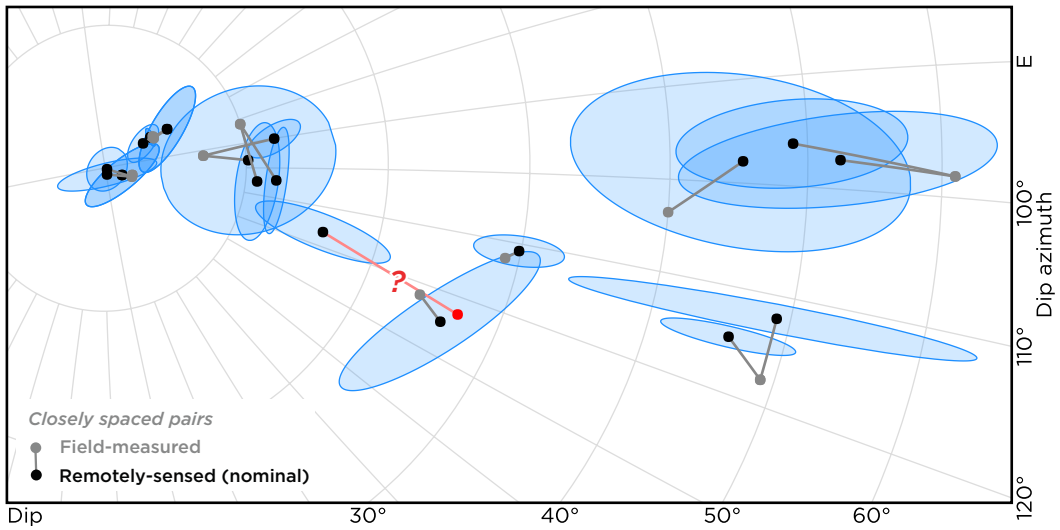

Figure 11: Upper-hemisphere stereonet showing poles to bedding for pairs of closely spaced field- and remotely-measured bedding orientations in the San Rafael Swell [Figure 9]. Errors generally increase at steeper dips (towards the right). One literature measurement (highlighted with a red ? and corresponding to the same symbol in Figure 9d) is steeper than all nearby remotely-sensed dips and does not conform to the regional structural pattern, suggesting that it may be an error in the preparation of the geologic map.

stratigraphic section of the Zebra Nappe above this basal thrust fault (*Quinn and Grotzinger*, 2016). Using UAV imagery gathered during this field study [Figure 12a], we construct a coarse-resolution digital outcrop model of this area [Figure 12a]; this dataset is used to test the recovery of bedding orientations by the techniques described in this paper. Assessing the quality of measurements by UAVs is of significant interest for terrestrial field geological studies (e.g. *Cawood et al.*, 2017), and multi-view aerial data tests the functionality of the method with off-vertical errors and ad-hoc photogrammetry that characterize UAV-based surface model creation.

4.2.1 Datasets An 80-meter elevation range within the ~300 m cliff face at Onis Farm was chosen for this comparison, comprising the upper Ubisis Formation, the Tsams Formation, and the lower Lemoenputs Formation of the Zebra Nappe; field structural data was subset from a stratigraphic dataset assembled for the entire cliff (*Quinn and Grotzinger*, 2016). Within the target elevation range, bedding orientation measurements were collected at six locations with a Brunton compass clinometer, and the GPS position and description of the measured bed were logged [Figure 12]. The elevation of each measurement was determined after measurement by draping the georeferenced data atop an Advanced Land Observing Satellite (ALOS) global 15-m resolution photogrammetric DEM, which was used as a regional topographic basemap.

Outcrop images were acquired for processing into a 3D model using a remotely piloted DJI Phantom 4 quadcopter UAV, from an altitude of ~200 m above ground and ~500-800 m lateral standoff southeast of the target cliff. The aircraft was approximately level with the target strati-

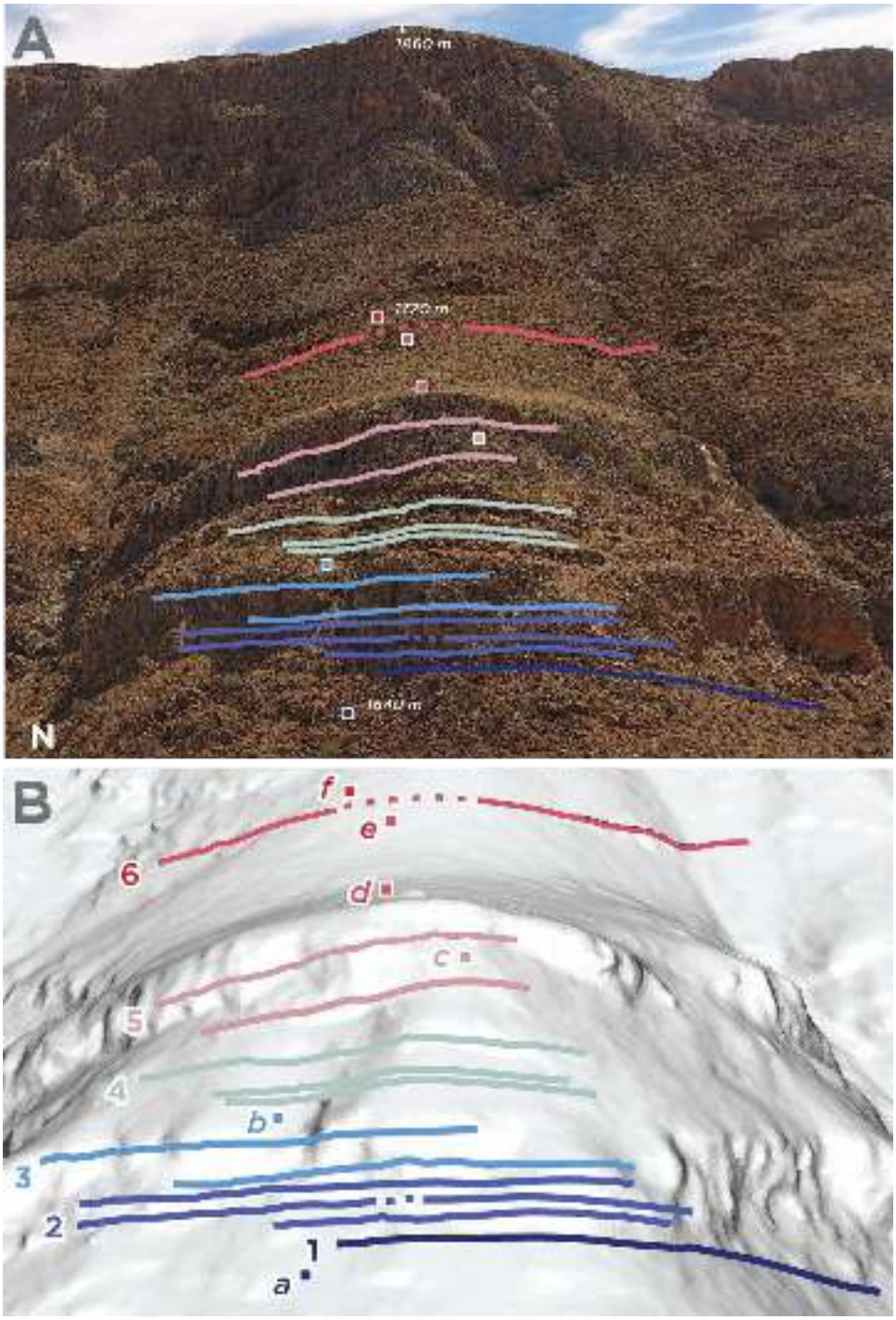

Figure 12: **(a)** UAV photograph (~500 m standoff) looking NW towards the cliffs at Onis Farm, Naukluft Mountains, Namibia. Digitized bedding traces (colored lines) and the locations of field-measured orientations (colored squares) are superposed. Beds dip ~30-45° degrees into the hillslope (away from viewer). 230 m of topographic relief is shown in the photo. **(b)** Digital surface model from UAV photogrammetry, viewed from slightly below the viewpoint of panel *a*, with digitized bedding traces superposed. Bedding traces grouped for analysis are connected by dashed lines. Groups of bedding traces with similar properties are numbered 1-6; field-measured orientations are lettered *a-f*.

graphic interval [Figure 12a]. UAV images were combined into a photogrammetric 3D model using the Agisoft Photoscan Professional v1.2 structure-from-motion software package [Figure 12b]. The 3D model was assembled with the "very high" quality setting and has ~4 million constituent points and a horizontal resolution of ~15 cm per pixel. The model extends ~1.5 km laterally along the cliff face and captures ~400 m of relief on the east-facing cliff. The model has an approximate horizontal resolution of 15 cm per pixel, though precision on all axes varies within the scene depending on the stereo convergence geometry of individual image pairs.

The stratigraphic interval studied contains two cliff faces with intervening float-covered slopes; beds traceable in UAV imagery primarily occur on the cliffs. The traces of 14 bedding surfaces were digitized manually in Agisoft Photoscan atop oblique images registered to the 3D model [Figure 12]. Agisoft Photoscan automatically drapes digitized bedding traces onto the surface model, creating a 3D point dataset without an additional software package or conversion to a gridded DEM. Digitized bedding traces were exported as a `dxf`-format file using the UTM Zone 33S coordinate system. The `fiona` Python module was used to read this data, and the `attitude` software package was used for planar fitting. Four bedding traces were grouped with other traces at similar stratigraphic levels to increase statistical power, yielding a final set of 12 distinct orientation measurements. An `iPython` notebook containing the analytical pipeline for this example is available as supplementary material to this publication.

4.2.2 UAV and field data comparison Field-measured bedding orientations for the target stratigraphic interval range in strike from 225-245°, corresponding to dip azimuths of 315-335°. Dips range from 30 to 45° to the northwest (into the hillslope). Field-measured orientations are lettered *a-f*, and sets of remotely-sensed measurements are numbered 1-6 [Figure 12b and Figure 13].

The lowest-elevation extracted bedding trace (1) follows a coarse sandstone bed across the nose of the hillslope. Its orientation is well-constrained, with a maximum angular error of ~5°, but significantly different from the field-measured orientation of a siltstone bed ~10 m stratigraphically below (*a*). This mismatch may result from an actual dip change due to slight folding across the lithologic boundary at the base of the cliff.

The next intervals (2 and 3) contain five beds within a dolomite cliff; two of these measurements were grouped. The beds in 2 and 3 have error ellipses elongated in the dip direction, representing measurements well-constrained on a single axis (roughly, their apparent dip in standoff imagery); their error spaces overlap that of (1), suggesting consistent bedding orientations for the entire lower cliff.

Beds marked as 4 occur in a fine–medium sandstone interval where stairstep beds are easily traced; these beds are individually well-resolved and generally steeper than the beds of 2 and 3. These measurements closely correspond to field measurement *b* in dip but suggest a strike ~5° to the west. Since several remotely-sensed beds agree closely, this rotation may be caused by a slight

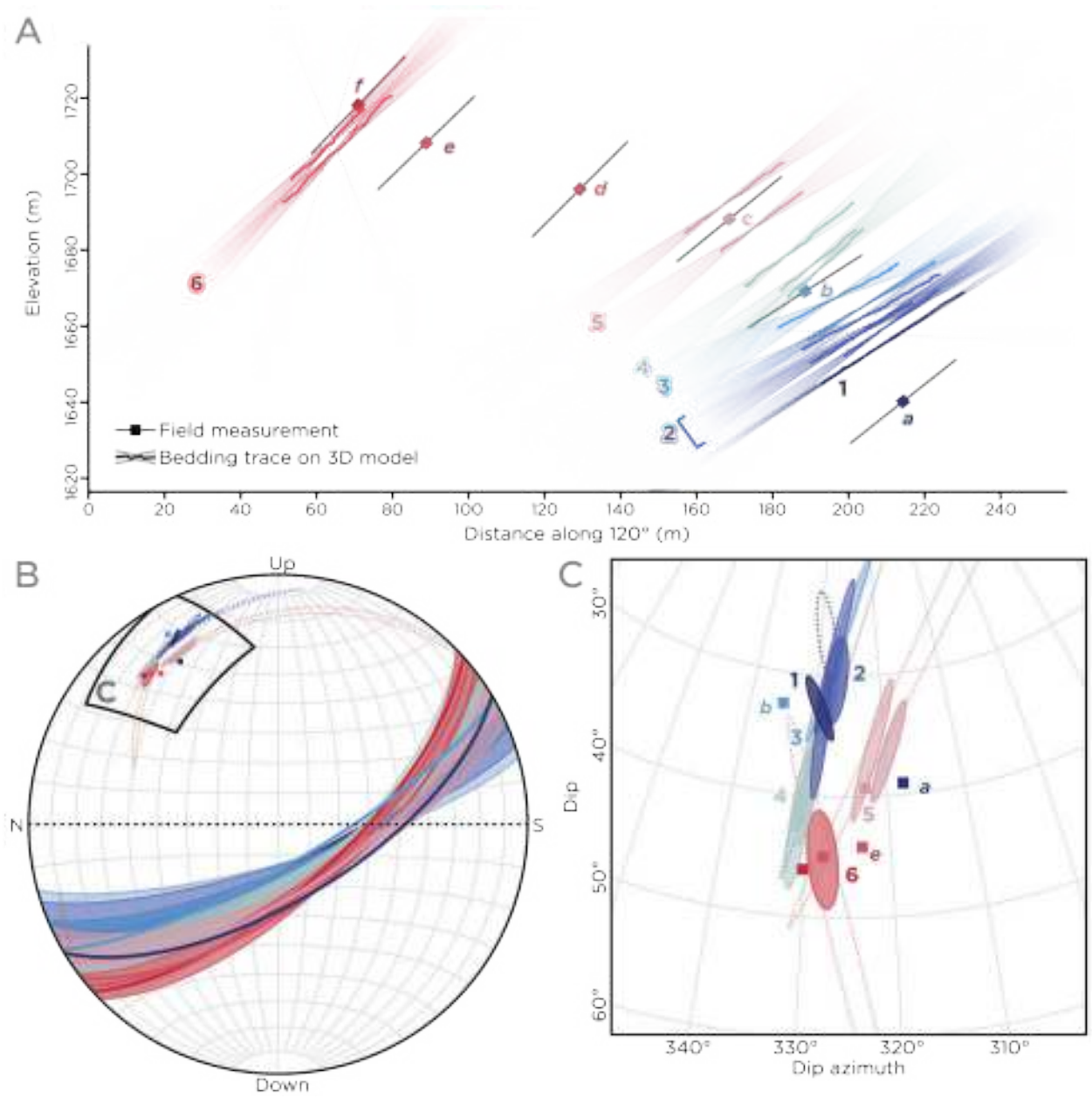

Figure 13: Comparison of field-measured and UAV photogrammetric bedding orientations for the Onis cliffs. Remotely-sensed and field-measured bedding orientations are colorized by height. In each panel, error spaces for individual remotely-sensed measurements are shown as colored fields. Dotted lines show the error bounds of measurements prior to grouping. **(a)** Orthographic projection of bedding orientations, with the horizontal axis showing distance to the southeast, approximately along the dip direction measured beds Remotely-measured beds are shown as residuals to their best-fitting plane and overlain by hyperbolic error bounds. The recovery of dips into the hillslope by remotely-sensed orientations is apparent. **(b)** Upper-hemisphere oblique equal-area stereonet showing NW-dipping bedding girdles for remotely-sensed and field measurements. Dotted lines represent the edges of error ellipses for components of grouped measurements. **(c)** Errors to poles of bedding, showing close correspondence with field measurements (squares) and the orientation of maximum errors in dip.

error in field measurement.

Beds in 5 were measured in a dolomite cliff, and the extracted error distributions overlap the field measurement *c* within the same interval, suggesting orientation reconstruction to within a few degrees. Field measurements *d*, *e*, and *f* were measured on a float-covered slope of the Lemoenputs Formation with few traceable bedding planes. One somewhat resistant dolomite bed (6) can be traced on both sides of the hillslope but not over its nose. When grouped, these measurements outline a single plane dipping at ~45° that corresponds closely in orientation to *d*, *e*, and *f*.

Bedding orientations extracted from the UAV dataset correspond closely to field-measured orientations, recording bedding dips 30-50° northwest (into the hillslope) and steepening with elevation. In general, strike is constrained to within a few degrees, while dips are constrained to within ~5-15°. This error structure is consistent with the relatively stronger constraints on apparent dips along the cliff face than dips in and out of the cliff. Flights only on a single side of a relatively planar outcrop entail little 3D structure with which to derive well-constrained orientations. However, even with a relatively low-resolution (15 cm/pixel) SfM photogrammetric elevation model, the crucial observation of beds steeply dipping into the outcrop is easily captured.

5 Potential future improvements to the statistical framework

5.1 Modeling data with different error structures

The statistical error bounds developed for unweighted PCA regression in Section 3.3 are general and adaptable to a wide variety of data types. Different statistical frameworks can be substituted, and supplements to this statistical framework can be used to model errors for uncertain orientations using situation-specific information as described below.

5.1.1 Adding a noise floor PCA-based regression is responsive to the scale of errors, but known errors in the input data are not automatically accounted for in the fitting process. If there exists a measure of data input error, a "noise floor" can be imposed that defines a minimum amount of noise expected for the input dataset. This can be accomplished by conditionally replacing λ_3 in Equation 23 with a standard value for the minimum noise variance, to ensure that $\lambda_3 \geq \min \sigma^2_{\hat{\mathbf{M}}}$.

For instance, if the accuracy of a point cloud is 1 m, as computed based on external criteria (e.g. the input stereo geometry of a gridded elevation model or measurement error for LIDAR or radar ranging), introducing a noise floor of $\min \sigma^2_{\hat{\mathbf{M}}} = 1$ into calculations of the noise covariance could correct for false certainty arising from possible local smoothing of data.

5.1.2 Rescaling error sensitivity An advantage of the isotropic error framework of PCA is its flexibility: because coordinates are not fixed, the input dataset can be rescaled along any axis. Different axial weightings can be a useful way to incorporate known errors on single-axis param-

eters of the input data (e.g. photogrammetric image-registration errors).

This property can be used to control the relative sensitivity of the fit to errors along each axis of the input data. It is often desirable to set error sensitivities separately based on informed criteria around dataset-specific error sources (*Carroll and Ruppert*, 1996). For instance, orbital photogrammetric DEMs might be tuned for chiefly vertical errors, while oblique SfM photogrammetry would be given higher sensitivity in the oblique view direction. While our current statistical framework treats errors along all axes equally, the software can be modified to fit different errors along each axis. The PCA framework can be limited to only vertical errors, mimicking OLS, or utilized in a variety of other weighted schemes (e.g. *Friendly et al.*, 2013; *Francq and Govaerts*, 2014).

5.1.3 Applying other statistical models In addition to the asymptotic Gaussian and noise-based statistical models described in this paper [Section 3.3.3], numerical methods such as bootstrap resampling and Monte Carlo sensitivity analysis can also be used to generate high-quality errors in the fit parameters of the plane. These methods are numerically intensive and difficult to generalize, but allow the incorporation of detailed assumptions about dataset errors. Additionally, a variety of situation-specific statistical techniques can be substituted for PCA, such as OLS and weighted schemes described above. No matter which statistical framework is used, the fitting and data-visualization methods described outlined in this paper can be used to represent uncertain planes.

5.2 The link with Bingham statistics

The Bingham statistical distribution is a generalized statistical distribution of undirected orientations (*Bingham*, 1974). The core assumption of the Bingham framework is that for the axes of a distribution $\mathbf{a}$, $\mathrm{trace}(\mathbf{a}^2) = 1$. Applying the Bingham transformation to a Cartesian set of error axes is functionally equivalent to finding the tangents to a hyperbolic error range. As such, our hyperbolic axes $\mathbf{h}$ can be transformed into the Bingham structural parameters κ_1 and κ_2 (*Bingham*, 1974; *Onstott*, 1980).

When fully explored, the formal link between PCA regression and Bingham statistics will allow uncertain orientation measurements to be treated as probability density functions in spherical space. This will allow higher-level statistical transforms to be applied to measurements, including combination using error-propagation techniques, and the application of statistical significance tests. Formalizing the conceptual link between Cartesian and Bingham statistics may unlock new potential applications for this error-analysis framework.

6 Conclusion and recommendations

We have described a complete error-analysis workflow for the orientation of geological planes, especially stratigraphic bedding, that improves on typical regression statistics for the assessment of geological planes. Our PCA-based analysis includes a regression method, a framework

for statistically-based errors, mathematical approaches for the 2D visualization and reporting of structural data with errors, and software to handle calculations and data management.

As shown by the two terrestrial examples, these analytical procedures are generalized and flexible. They can be used to model the orientation of planes on map-projected satellite and aerial imagery, as well as digital surface models built with LIDAR, UAV photogrammetry, and radar techniques. Application of the error analysis method in the San Rafael Swell successfully captures the structural pattern of this geological area. The relatively good conformance with in-situ measurements was gained despite the use of off-the-shelf data products, reflecting the flexibility and wide applicability of this method to readily available nadir-looking imagery and elevation datasets. Application of the method to oblique-looking UAV data on the Naukluft plateau demonstrated the viability of PCA-based orientation calculation in a reconnaissance study using high-obliquity aerial imagery with relatively inexpensive equipment and SfM photogrammetry software.

The coupling of a robust error-analysis framework with techniques to visualize the error space allows simple and transparent analytical workflows. Error-minimizing data collection strategies can be easily compared, and heterogeneous data can be used with full knowledge of the errors involved. We propose a standardized method for numerical reporting of uncertain planar orientations, combining the basic strike/dip representation with terms for angular errors on two axes, and the rake of these error axes within the best-fitting plane [Section 2], and yielding [*strike, dip, rake, min. angular error, max. angular error*] for each measurement. Additionally, we create intuitive stereonet display methods that provide a natural means to visualize uncertain planar orientations alongside traditional structural data.

Overall, the results of this study suggest that errors arising from outcrop geometry are at least as important as precision of the input remote-sensing dataset in defining the error space of a fitted plane. Traces of geologic features can only be modeled as unique planes when they query a three-dimensional point dataset, and error structures for different outcrops can be completely different within the same dataset. For characterization of orientations in an outcrop, we recommend that care be taken to find beds that sample a wide range of hillslope aspect or depth within an obliquely-measured scene (or groups of closely-spaced beds that collectively sample such a range). Furthermore, we suggest that digitizing precision is of subsidiary importance to collecting such a varied sample set: small errors in describing a fitted plane are will not significantly diminish the quality of the fit relative to poor sampling of three-dimensional outcrop variability. Thus, measuring a large quantity of adjacent bed surfaces provides the best opportunity to remove poor measurements and group incomplete ones.

We expect the methods described here will push the scale of geologic inference towards the resolution limit of 3D surface models, broadening the range of structural interpretations that can be made from remotely sensed imagery. This will increase the fidelity of structural measure-

ments supported by UAVs and LIDAR scanners in terrestrial research, rover-based cameras for *in-situ* planetary exploration, and satellite data for regional planetary mapping. To that end, we release the software we developed to implement these methods and visualize strike and dip in the Appendix.

7 Acknowledgements

We would like to thank NASA for the NASA Earth and Space Science Fellowship to D.P. Quinn that funded this work. Our software tools are archived with CaltechDATA (*DOI not yet created*) in conjunction with this work. Data for the examples shown in the paper is part of the testing suite for the `attitude` software package.

Bibliography

Babamoradi, H., F. Van Den Berg, and . Rinnan (2013), Bootstrap based confidence limits in principal component analysis - A case study, *Chemometrics and Intelligent Laboratory Systems*, *120*, 97–105, doi:10.1016/j.chemolab.2012.10.007.

Bingham, C. (1974), An Antipodally Symmetric Distribution on the Sphere, *The Annals of Statistics*, *2*(6), 1201–1225, doi:10.1214/aos/1176342874.

Buckley, S. J., J. Howell, H. Enge, and T. Kurz (2008), Terrestrial laser scanning in geology: Data acquisition, processing and accuracy considerations, *Journal of the Geological Society*, *165*(3), 625–638, doi:10.1144/0016-76492007-100.

Carroll, R. J., and D. Ruppert (1996), The Use and Misuse of Orthogonal Regression in Linear Errors-in-Variables Models, *The American Statistician*, *50*(1), 1–6, doi:10.1080/00031305.1996.10473533.

Cawood, A. J., C. E. Bond, J. A. Howell, R. W. Butler, and Y. Totake (2017), LiDAR, UAV or compass-clinometer? Accuracy, coverage and the effects on structural models, *Journal of Structural Geology*, *98*, 67–82, doi:10.1016/j.jsg.2017.04.004.

Cruden, D. M., and H. A. K. Charlesworth (1976), Errors in strike and dip measurements, *Bulletin of the Geological Society of America*, *87*(7), 977–980, doi:10.1130/0016-7606(1976)87<977:EISADM>2.0.CO;2.

DiBiase, R. A., A. B. Limaye, J. S. Scheingross, W. W. Fischer, and M. P. Lamb (2013), Deltaic deposits at Aeolis Dorsa: Sedimentary evidence for a standing body of water on the northern plains of Mars, *Journal of Geophysical Research: Planets*, *118*(6), 1285–1302, doi:10.1002/jgre.20100.

Doelling, H., P. Kuehne, G. Willis, and J. Ehler (2017), Geologic map of the San Rafael Desert 30' x 60' quadrangle, Emery and Garfield Counties, Utah.

Dromart, G., C. Quantin, and B. Olivier (2007), Stratigraphic architectures spotted in southern Melas Chasma, Valles Marineris, Mars, *Geology*, *35*(4), 363–366, doi:10.1130/G23350A.1.

Edgar, L., J. P. Grotzinger, A. G. Hayes, D. M. Rubin, S. W. Squyres, J. F. Bell, and K. E. Herkenhoff (2012), Stratigraphic architecture of bedrock reference section, Victoria crater, Meridiani Planum, Mars, in *Sedimentary Geology of Mars*, edited by J. P. Grotzinger and R. E. Milliken, SEPM (Society for Sedimentary Geology), doi:10.2110/pec.12.102.

Faber, K., and B. R. Kowalski (1997), Propagation of measurement errors for the validation of predictions obtained by principal component regression and partial least squares, *Journal of Chemometrics*, *11*(3), 181–238, doi:10.1002/(SICI)1099-128X(199705)11:3<181::AID-CEM459>3.0.CO;2-7.

Faber, N. M., L. Buydens, and G. Kateman (1993), Standar Errors in the Eigenvalues of a Cross-Product Matrix: Theory and Applications, *Journal of Chemometrics*, *7*, 495–526, doi:10.1063/1.3033202.

Faber, N. M., M. J. Meinders, P. Geladi, M. Sjöström, L. M. C. Buydens, and G. Kateman (1995), Random error bias in principal component analysis. Part I. derivation of theoretical predictions, *Analytica Chimica Acta*, *304*(3), 257–271, doi:10.1016/0003-2670(94)00585-A.

Fahrmeir, L., T. Kneib, S. Lang, and B. Marx (2013), *Regression: Models, Methods, and Applications*, Springer-Verlag, Berlin Heidelberg.

Fienen, M. N. (2005), The Three-Point Problem , Vector Analysis and Extension to the N-Point Problem, *Journal of Geoscience Education*, *53*(3), 257–263, doi:10131402110716480.

Fisher, N. I., T. Lewis, and B. J. Embleton (1987), *Statistical Analysis of Spherical Data*, Cambridge university press.

Fraeman, A. A., R. E. Arvidson, J. G. Catalano, J. P. Grotzinger, R. V. Morris, S. L. Murchie, K. M. Stack, D. C. Humm, J. a. McGovern, F. P. Seelos, K. D. Seelos, and C. E. Viviano (2013), A hematite-bearing layer in Gale Crater, Mars: Mapping and implications for past aqueous conditions, *Geology*, *41*(10), 1103–1106, doi:10.1130/G34613.1.

Francq, B. G., and B. B. Govaerts (2014), Hyperbolic confidence bands of errors-in-variables regression lines applied to method comparison studies, *Journal de la Société Française de Statistique*, *155*(1), 23–45.

Friendly, M., G. Monette, and J. Fox (2013), Elliptical Insights: Understanding Statistical Methods through Elliptical Geometry, *Statistical Science*, *28*(1), 1–39, doi:10.1214/12-STS402.

Gesch, D. B., M. J. Oimoen, and G. A. Evans (2014), Accuracy assessment of the US Geological Survey National Elevation Dataset, and comparison with other large-area elevation datasets: SRTM and ASTER, *Tech. rep.*, US Geological Survey.

Gilluly, J., and J. B. Reeside Jr (1928), Sedimentary rocks of the San Rafael Swell and some adjacent areas in eastern

Utah, *Tech. Rep. 150-D*.

Goudge, T. A., R. E. Milliken, J. W. Head, J. F. Mustard, and C. I. Fassett (2017), Sedimentological evidence for a deltaic origin of the western fan deposit in Jezero crater , Mars and implications for future exploration, *Earth and Planetary Science Letters*, *458*, 357–365, doi:10.1016/j.epsl.2016.10.056.

Jolliffe, I. T. (2002), Principal Component Analysis, *Springer Series in Statistics*, *98*, 487, doi:10.1007/b98835.

Kent, J., J. Briden, and K. Mardia (1983), Linear and planar structure in ordered multivariate data as applied to progressive demagnetization of palaeomagnetic remanence, *Geophysical Journal of the Royal Astronomical Society*, *75*(3), 593–621, doi:10.1111/j.1365-246X.1983.tb05001.x.

Kirschvink, J. L. (1980), The least-squares line and plane and the analysis of paleomagnetic data, *Geophysical Journal of the Royal Astronomical Society*, *62*(3), 699–718, doi:10.1111/j.1365-246X.1980.tb02601.x.

Kite, E. S., K. W. Lewis, M. P. Lamb, C. E. Newman, and M. I. Richardson (2013), Growth and form of the mound in Gale Crater, Mars: Slope wind enhanced erosion and transport, *Geology*, *41*(5), 543–546, doi:10.1130/G33909.1.

Kite, E. S., J. Sneed, D. P. Mayer, K. W. Lewis, T. I. Michaels, A. Hore, and S. C. Rafkin (2016), Evolution of major sedimentary mounds on Mars: Buildup via anticompensational stacking modulated by climate change, *Journal of Geophysical Research: Planets*, *121*(11), 2282–2324, doi:10.1002/2016JE005135.

Lewis, K., O. Aharonson, and J. Grotzinger (2008a), Quasi-Periodic Bedding in the Sedimentary Rock Record of Mars, *Science*, *1532*(2008), doi:10.1126/science.1161870.

Lewis, K. W., and O. Aharonson (2006), Stratigraphic analysis of the distributary fan in Eberswalde crater using stereo imagery, *Journal of Geophysical Research*, *111*(E6), 1–7, doi:10.1029/2005JE002558.

Lewis, K. W., and O. Aharonson (2014), Occurrence and origin of rhythmic sedimentary rocks on Mars, *Journal of Geophysical Research: Planets*, *119*(6), 1432–1457, doi:10.1002/2013JE004404.

Lewis, K. W., O. Aharonson, J. P. Grotzinger, S. W. Squyres, J. F. Bell, L. S. Crumpler, and M. E. Schmidt (2008b), Structure and stratigraphy of home plate from the spirit mars exploration rover, *Journal of Geophysical Research: Planets*, *113*(E12).

Malin, M. C., and K. S. Edgett (2000), Sedimentary Rocks of Early Mars, *Science*, *290*(5498), 1927–1937, doi:10.1126/science.290.5498.1927.

Malinowski, E. (1977), Theory of error in factor analysis, *Analytical Chemistry*, *49*(4), 606–612, doi:10.1021/ac50012a026.

Mardia, K. V. (2014), *Statistics of Directional Data*, Academic press.

McEwen, A. S., M. C. Malin, M. H. Carr, and W. K. Hartmann (1999), Voluminous volcanism on early Mars revealed in Valles Marineris, *Nature*, *397*(6720), 584–586, doi:10.1038/17539.

Metz, J., J. Grotzinger, C. Okubo, and R. Milliken (2010), Thin-skinned deformation of sedimentary rocks in Valles Marineris, Mars, *Journal of Geophysical Research E: Planets*, *115*(11), 1–28, doi:10.1029/2010JE003593.

Nurunnabi, A., D. Belton, and G. West (2012), Diagnostic-robust statistical analysis for local surface fitting in 3D point cloud data, *ISPRS Annals of the Photogrammetry Remote Sensing and Spatial Information Sciences*, *I-3*(September), 269–274, doi:10.5194/isprsannals-I-3-269-2012.

Okubo, C. H. (2010), Structural geology of Amazonian-aged layered sedimentary deposits in southwest Candor Chasma, Mars, *Icarus*, *207*(1), 210–225, doi:10.1016/j.icarus.2009.11.012.

Okubo, C. H., K. W. Lewis, A. S. McEwen, and R. L. Kirk (2008), Relative age of interior layered deposits in southwest Candor Chasma based on high-resolution structural mapping, *Journal of Geophysical Research*, *113*(E12), E12,002, doi:10.1029/2008JE003181.

Onstott, T. (1980), Application of the Bingham distribution function in paleomagnetic studies, *Journal of Geophysical Research: Solid Earth*, *85*(B3), 1500–1510, doi:10.1029/JB085iB03p01500.

Quantin, C., P. Allemand, N. Mangold, G. Dromart, and C. Delacourt (2005), Fluvial and lacustrine activity on layered deposits in Melas Chasma, Valles Marineris, Mars, *Journal of Geophysical Research E: Planets*, *110*(12), 1–18, doi:10.1029/2005JE002440.

Quinn, D. P., and B. L. Ehlmann (2018), The deposition and alteration history of the northeast Syrtis layered sulfates, *Journal of Geophysical Research: Planets*, (submitted).

Quinn, D. P., and J. P. Grotzinger (2016), Stratigraphy and sedimentology of the Zebra Nappe, Naukluft Nappe Complex, Namibia, *Geological Society of America Abstracts with Programs*, *48*(7), doi:10.1130/abs/2016AM-287992.

Richter-Gebert, J. (2011), Conics and their duals, in *Perspectives on Projective Geometry: A Guided Tour Through Real and Complex Geometry*, pp. 145–166, Springer Berlin Heidelberg, Berlin, Heidelberg, doi:10.1007/978-3-642-17286-1_9.

Rowe, C. D., J. C. Fagereng, J. a. Miller, and B. Mapani (2012), Signature of coseismic decarbonation in dolomitic fault rocks of the Naukluft Thrust, Namibia, *Earth and Planetary Science Letters*, *333-334*, 200–210, doi:10.1016/j.epsl.2012.04.030.

Schröcker, H.-P. (2007), Minimal Enclosing Hyperbolas of Line Sets, *Contributions to Algebra and Geometry*, *48*(2), 367–381.

Stack, K. M., C. S. Edwards, J. P. Grotzinger, S. Gupta, D. Y. Sumner, F. J. Calef, L. A. Edgar, K. S. Edgett, A. A. Fraeman, S. R. Jacob, L. Le Deit, K. W. Lewis, M. S. Rice, D. Rubin, R. M. E. Williams, and K. H. Williford (2015), Comparing orbiter and rover image-based mapping of an ancient sedimentary environment, Aeolis Palus, Gale crater, Mars, *Icarus*, *280*, 3–21, doi:10.1016/j.icarus.2016.02.024.

Tipping, M. E., and C. M. Bishop (1999), Mixtures of probabilistic principal component analyzers., *Neural computation*, *11*(2), 443–482, doi:10.1162/089976699300016728.

Vollgger, S. A., and A. R. Cruden (2016), Mapping folds and fractures in basement and cover rocks using UAV photogrammetry, Cape Liptrap and Cape Paterson, Victoria, Australia, *Journal of Structural Geology*, *85*, 168–187.

Weingarten, J., G. Gruener, and R. Siegwart (2004), Probabilistic plane fitting in 3D and an application to robotic mapping, *IEEE International Conference on Robotics and Automation*, *1*(April), 927–932, doi:10.1109/ROBOT.2004.1307268.

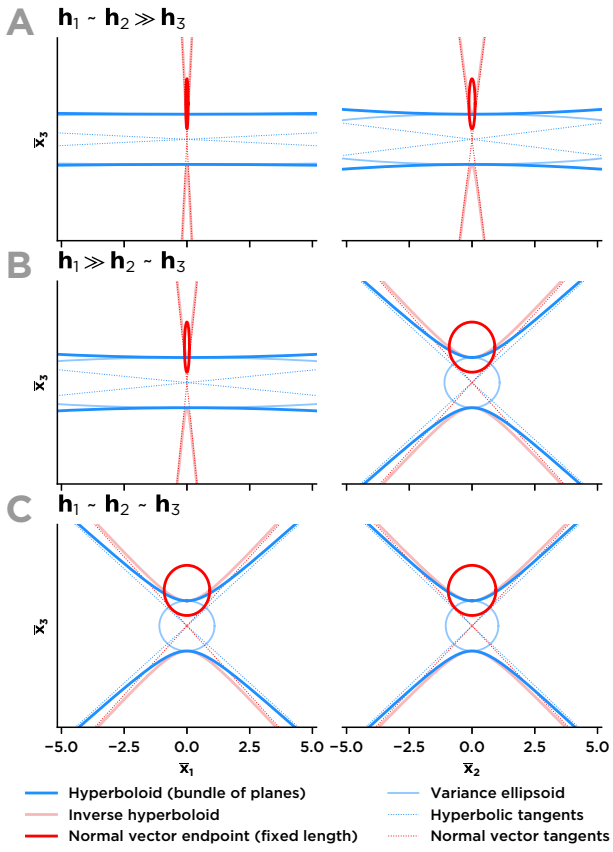

Figure 14: Several mathematically related constructions of the error space of a uncertain plane as hyperbolic quadrics and ellipsoids. Correspondence of the error space of a plane defined by semiaxes $\mathbf{h}$ with hyperbolic and ellipsoidal representations of the error space of the normal vector to the plane, showing angular scaling of the subtended area of these constructions depending on the ratio of the semiaxes.

Appendices

A Quadric representation of the orientation error space

We represent error surfaces for planar orientation measurements as 3D generalized conic sections, or quadric surfaces [Figure 2]. Planar fit errors can represented as matrices, plotted as quadrics, and translated between representations of the error space as hyperboloids, ellipsoids, and cones of tangency by linear algebraic methods, such as the geometric (e.g. affine and projective) transformations described below.

In three-dimensional space, an uncertain planar measurement is structured as a hyperboloid of two sheets (an elliptic hyperboloid), opening along the error axis (λ_3). Conceptually, this hyperboloid represents the minimal enclosing surface of a bundle of all possible planes corresponding to the regression (*Schröcker*, 2007). Another possible representation is as a bundle of possible normal vectors to the plane, which can be defined by a hyperboloid encompassing all vectors or an ellipsoid containing the endpoints of equal-length vectors [Figure 1]. Representation of errors in a normal-vector framework is less inherently meaningful than the hyperbolic construction, since normal vectors do not "contain" the modeled plane. However, the manipulation of uncertain vectors is simpler than uncertain planar bundles, and the vector representation of orientation errors

eases comparison and transformation [Figure 14].

A.1 A hyperboloid enclosing the plane

The axes h define a hyperboloid representing the errors to the planar fit, conforming to the general equation for an origin-centered hyperbola opening along $\overline{\mathrm{x}}_3$ of

$$\frac{\overline{\mathrm{x}}_1^2}{\mathrm{h}_1^2} + \frac{\overline{\mathrm{x}}_2^2}{\mathrm{h}_2^2} - \frac{\overline{\mathrm{x}}_3^2}{\mathrm{h}_3^2} = -1. \tag{37}$$

When incorporated into a 4×4 matrix representation of the PCA-aligned error quadric,

$$\overline{\mathbf{Q}}_{\mathbf{H}} = \mathrm{diag}([\tfrac{1}{\mathrm{h}_1^2}, \tfrac{1}{\mathrm{h}_2^2}, -\tfrac{1}{\mathrm{h}_3^2}, -1]), \tag{38}$$

forms part of a general equation for a quadric surface

$$\overline{\mathbf{x}}^{\mathrm{T}} \overline{\mathbf{Q}}_{\mathbf{H}} \overline{\mathbf{x}} = 0 \tag{39}$$

(e.g. *Richter-Gebert*, 2011).

This matrix representation allows manipulation of the error distribution in three dimensions. For example, the PCA-aligned error hyperboloid can be transformed into real space by sequentially applying two affine transformations to $\overline{\mathbf{Q}}_{\mathbf{H}}$: first a rotation into the real coordinate vectors with the augmented rotation matrix $\mathbf{V}_{\mathrm{A}}$ ($\mathbf{V}$ augmented with the 4×4 identity matrix) and translation defined by $\mathbf{T}_{\boldsymbol{\mu}}$, an identity matrix with a last column $[-\boldsymbol{\mu}_{\mathbf{D}}, 1]$, to shift the center of the coordinate system to the origin from the mean of the measured plane. Thus,

$$\mathbf{Q}_{\mathbf{H}} = (\mathbf{V}_{\mathrm{A}} \mathbf{T})^{\mathrm{T}} \overline{\mathbf{Q}}_{\mathbf{H}} \mathbf{V}_{\mathrm{A}} \mathbf{T}, \tag{40}$$

and the quadric representing the uncertain plane becomes

$$\mathbf{x}^{\mathrm{T}} \mathbf{Q}_{\mathbf{H}} \mathbf{x} = 0. \tag{41}$$

A.2 Errors to normal vectors

Errors to normal vectors can be defined as both a hyperboloid containing all possible normal vectors passing through the center of the plane, and an offset ellipsoid representing errors to a normal vector with fixed length. Projected from the origin, all error spaces for the normal vector subtend the same angle, equivalent but orthogonal to that subtended by $\overline{\mathbf{Q}}_{\mathbf{H}}$ [Figure 14].

The hyperbolic formulation of normal-vector errors is the "dual" quadric surface to $\overline{\mathbf{Q}}_{\mathbf{H}}$, related by inversion:

$$\overline{\mathbf{Q}}_{\mathbf{H}}' = \overline{\mathbf{Q}}_{\mathbf{H}}^{-1} = \mathrm{diag}([\mathrm{h}_1^2, \mathrm{h}_2^2, -\mathrm{h}_3^2, -1]). \tag{42}$$

This defines a hyperboloid of two sheets with a cone of tangency spanning the same angular distance as $\overline{\mathbf{Q}}_{\mathbf{H}}$, but normal to it. The hyperboloid defining normal vector error is a *point quadric*, dual tothe hyperbolic *plane quadric* surrounding the nominal value of the plane. Duality is a generalization of the concept of "inversion poles", which shows that for a given conic section, any interior point (a "pole") can be related to a unique reciprocal line outside the conic (a "polar") (*Richter-Gebert*, 2011).

A more intuitive ellipsoidal representation of the normal vector error space is arrived at when a fixed-length normal vector is assumed. Normal vector errors can be defined as an ellipsoid with semiaxes proportional to $\frac{1}{\mathrm{h}_i^2}$ and an arbitrary scale. For a normal vector of length $\sqrt{2}\mathrm{h}_3$, the ellipsoid semiaxes are scaled by a factor of h_3^2, resulting in an ellipsoid with major axes $[\frac{\mathrm{h}_3^2}{\mathrm{h}_1}, \frac{\mathrm{h}_3^2}{\mathrm{h}_2}, \mathrm{h}_3]$ with a center offset $\sqrt{2}\mathrm{h}_3$ from the origin along the 3 axis. This construction of the normal vector errors keeps the same relationship with the angular tangents to the normal vectors [Figure 14].

A.3 General method to map a quadric to a conic

Quadric surfaces can be sliced in any plane to form a 2D conic section. The ability to transform and slice the matrix representation of the error space along arbitrary axes allows the plotting of planar errors to single or multiple planes into common Cartesian coordinates for projection along arbitrary view axes [Figure 13].

Using a plane defined by two perpendicular vectors $\mathbf{v}_1$ and $\mathbf{v}_2$, and a point $\mathbf{a}$ within the plane, we can define a 4×3 transformation matrix to map the quadric down to a 2D conic section, stacking these vectors as columns, augmented with a final row $k = [0, 0, 1]$:

$$\mathbf{T} = \begin{bmatrix} \mathbf{v}_1 & \mathbf{v}_2 & \mathbf{a} \\ 0 & 0 & 1 \end{bmatrix}. \tag{43}$$

The conic section

$$\mathbf{C}_{\mathbf{H}} = \mathbf{T}^{\mathrm{T}} \mathbf{Q}_{\mathbf{H}} \mathbf{T} \tag{44}$$

defines the slice of the error space along that plane. The mapping to a hyperbolic slice of the error hyperboloid at any angle γ within the fitted plane can be found using the transformation matrix for axes $\overline{\mathrm{x}}_\gamma = [\cos\gamma, \sin\gamma, 0]$ and $\overline{\mathrm{x}}_3 = [0, 0, 1]$:

$$\mathbf{T} = \begin{bmatrix} \cos\gamma & 0 & 0 \\ \sin\gamma & 0 & 0 \\ 0 & 1 & 0 \\ 0 & 0 & 1 \end{bmatrix}. \tag{45}$$

For the simple case of the slice of the error space aligned with $\overline{\mathbf{x}}_1 = [1, 0, 0]$ and $\overline{\mathbf{x}}_3 = [0, 0, 1]$ and

centered at the origin, a transformation matrix

$$\mathbf{T} = \begin{bmatrix} 1 & 0 & 0 \\ 0 & 0 & 0 \\ 0 & 1 & 0 \\ 0 & 0 & 1 \end{bmatrix} \tag{46}$$

resolves

$$\mathbf{C_H} = \mathbf{T}^{\mathrm{T}}\overline{\mathbf{Q}}_{\mathbf{H}}\mathbf{T} = \mathrm{diag}([\tfrac{1}{\mathrm{h}_1^2},\ -\tfrac{1}{\mathrm{h}_3^2},\ 1]), \tag{47}$$

a hyperbola of two sheets, opening along h_3.

A.4 General method to move to spherical coordinates

A general representation for the tangents to the hyperbolic error spaces discussed above can be constructed as a cone of tangency, which can be easily transformed into spherical coordinates. This elliptic cone has the same semiaxes as the elliptic hyperboloid $\mathbf{Q_H}$ and can be represented as

$$\overline{\mathbf{Q}}_{\mathbf{T}} = \mathrm{diag}([\tfrac{1}{\mathrm{h}_1^2},\ \tfrac{1}{\mathrm{h}_2^2},\ -\tfrac{1}{\mathrm{h}_3^2}, 0]) \tag{48}$$

(with the last -1 in $\overline{\mathbf{Q}}_{\mathbf{H}}$ replaced with a 0). The orthogonal angular cone defining the normal vector can be found in general by inverting the cone of tangents $\overline{\mathbf{Q}}_{\mathbf{T}}$ to form

$$\overline{\mathbf{Q}}_{\mathbf{N}} = \mathrm{diag}([\mathrm{h}_1^2,\ \mathrm{h}_2^2,\ -\mathrm{h}_3^2,\ 0]). \tag{49}$$

B Software tools

We provide a software implementation that supports the orientation-analysis statistics and visualizations described here. The core software is the `attitude` Python module, which contains regression code and functions for importing point-based bedding traces from GIS data and other formats. This package also contains methods for plotting uncertain orientations in spherical coordinates using the Python libraries `matplotlib` and `cartopy`. The `attitude` module also includes a Javascript component implementing tools based on the `d3` visualization library for interactive stereonets and plots of decomposed axial variance. The Python and Javascript components can be used together in the **iPython Notebook** analytical environment, allowing interactive data inspection and exploratory grouping of jointly fitted planes, with minimal setup [Figure 15a]. The `attitude` module is open-source and available on GitHub (https://github.com/davenquinn/Attitude). Documentation and example notebooks are available at https://github.io/davenquinn/Attitude. Version 1.0 of the software and documentation has been archived with CaltechDATA in conjunction with this publication.

The `Orienteer` software application [Figure 15b] was created to ease the management of ori-

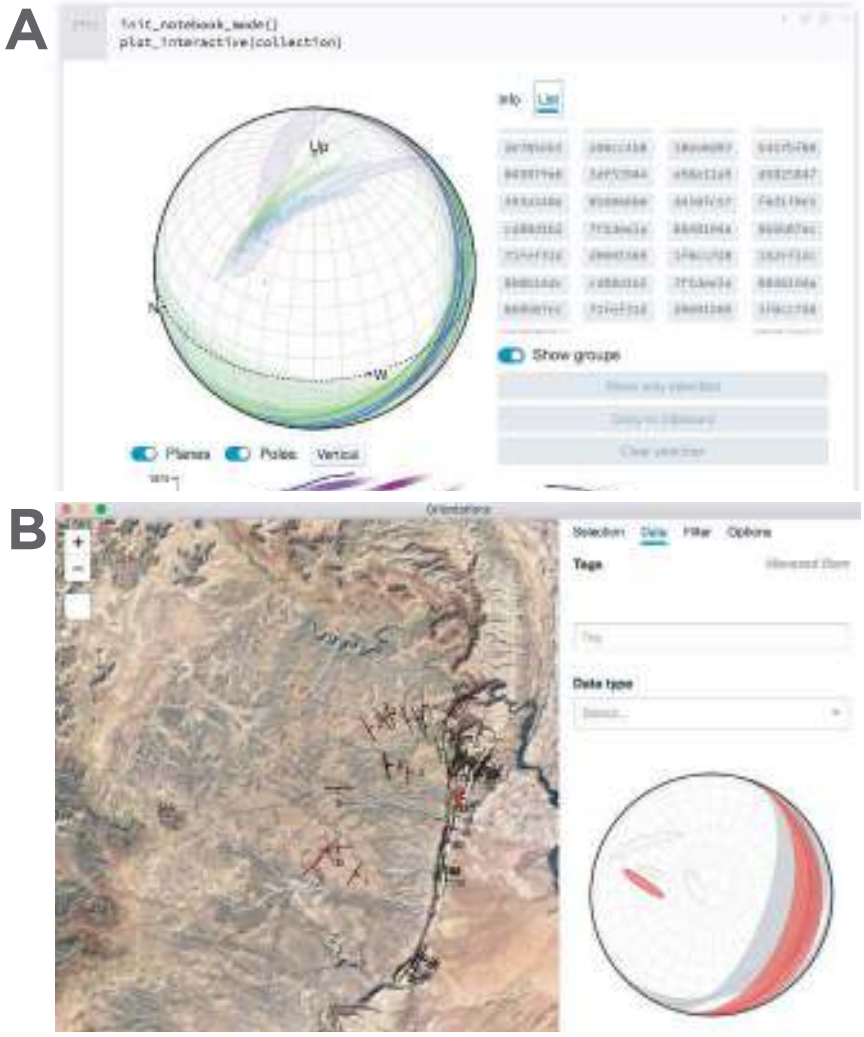

Figure 15: Screenshots of software developed in this study. **(a)** The `attitude` Python module running in an *iPython* notebook. **(b)** The *Orienteer* application in use for filtering a database of orientations atop Google Maps data for the San Rafael Swell, Utah.

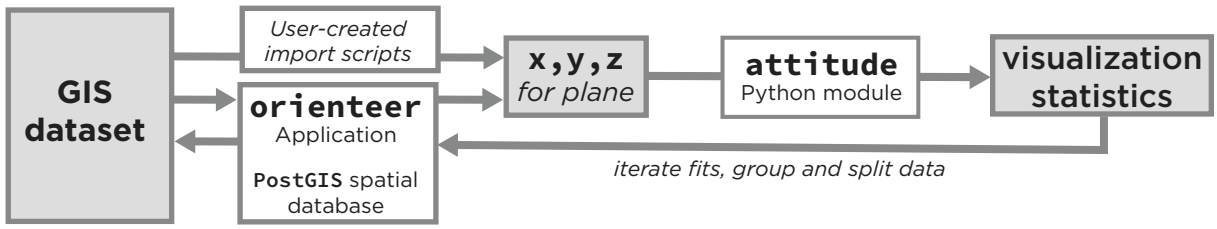

Figure 16: Workflow diagram showing the roles of the `attitude` Python module and `Orienteer` data-management application in an orientation-measurement software project. The `attitude` module supports a linear process flow, while the `Orienteer` application enables the management of orientation data across a large mapping project.

entation data over a large mapping project. This cross-platform desktop application interfaces with the `attitude` module and supports the management of orientation measurements and their underlying raster elevation models in a `PostGIS` spatial database. This application eases the filtering of planes by quality and grouping and splitting to assess the viability of joint fitting for data reduction, and serves as a companion to GIS software [Figure 16]. Although `Orienteer` adds powerful data management capabilities to the `attitude` software, it is more difficult to set up, requiring a `PostgreSQL` server, and is somewhat unstable due to its relative complexity. This application is also open-source and is available on GitHub (https://github.com/davenquinn/Orienteer) as well as archived with CaltechDATA in conjunction with publication.

The statistical method developed here can be expressed with basic linear algebra and should be straightforward to implement in programming environments such as MATLAB or R. Test cases are provided with the `attitude` module that can be used to verify accuracy. Additionally, since both QGIS and ArcGIS expose Python bindings, it is possible to use the `attitude` module directly within standard GIS software.